UNIVERSIDADE DE LISBOA
FACULDADE DE CIÊNCIAS
DEPARTAMENTO DE FÍSICA

Evaluation of Left Ventricle Strains by applying SPAMM cardiac MRI techniques

Vera Alexandra Fernandes Colaço

Mestrado Integrado em Engenharia Biomédica e Biofísica
Perfil em Radiações em Diagnóstico e Terapia

Dissertação orientada por:
Prof. Doutora Rita Nunes
Prof. Doutor Hugo Ferreira

2017

Aknowledgments

Firstly, I would like to express my deep gratitude to my supervisors Prof. Rita Nunes and Prof. Hugo Ferreira, and to my advisor Prof. Lenka Lhotska for the continuous support of my study and related research. Their motivation and enormous knowledge truly helped me during the planning and development of this research work. Their willingness to give their time so generously has been very much appreciated. I could not have imagined having better advisors for my Master Thesis.

My special thanks to Prof Jiří Hozman for his guidance and constructive suggestions and for kindly providing me all the data I needed to work with.

My very great appreciation to all the Professors from IBEB (Instituto de Biomédica e Engenharia Biofísica). Thank you for your enthusiastic encouragement and for being so supportive during my academic journey.

I also want to thank to my classmates from Faculdade de Ciências da Universidade de Lisboa and Instituto Superior Técnico da Universidade de Lisboa for the good times spent and for all the help. A special thanks to two of my closest friends Manuela Chen and Uzma Satar for being so kind and caring since the beginning and for the fun we have had in the last five years.

I also want to express special gratitude to my parents and all my family for all the help, patience, care and encouragement they have given me during my entire life. They were always present and supportive through all the stages in my academic journey. Without them, it would not be possible to reach this goal!

Last but not the least, I want to thank to my boyfriend João for all the support and care during this thesis and to my friends Mariana, Vera, Joana, Vanessa, Ana and Rita for always being there for me. I also want to thank to all my friends I met in Prague, Helen, Kuriakh, Brigitte, Hugo, Roxanna, Cigin, Diana, Maxi, Mira, Lisa, Michal, Ilya and Alba for all the great moments we spent and I will never forget.

Abstract

Cardiovascular diseases are one of the main causes of death in the world. These diseases modify the myocardial wall contraction during cardiac cycle. One of the most common types of these diseases is the dilated cardiomyopathy (DCM), in which the heart muscle becomes weaker and the heart cavities are enlarged. Consequently, the heart deformation capability is decreased, which prevents it from pumping blood efficiently. This condition can be genetic or due to various causes such as viral infections, inflammation or injuries.

The analysis of cardiac wall deformation enables identifying normal or abnormal deformations due to heart disease. Cardiac Magnetic Resonance Imaging (MRI) is able to detect the characteristic abnormalities of DCM, which are the wall thinning and dilation of heart chambers, more specifically the increasing of ventricle diameter. The result is a significant decrease in wall stress and strain, which has a negative impact on systolic ventricular performance. The Spatial Modulation of Magnetization (SPAMM) technique has been proposed for imaging myocardial motion within the plane of the image by creating a pattern of lines or grids with altered magnetization on the image. These patterns are tags that deform according to the heart muscle deformation and can be detected and tracked for wall motion studying.

The sample used in this thesis was composed by cardiac MRI scans of 9 subjects, 3 of which were healthy subjects and the other 6 were patients with DCM. The scans were acquired by Motol Hospital in Prague (Czech Republic) and analyzed in the Institute of Informatics, Robotics and Cybernetics from the Faculty of Electrical Engineering in Prague. The proposed thesis intended to assess the left ventricle (LV) radial and circumferential strains by automatically detecting LV tags and tracking those during cardiac cycle. By analyzing the heart strains from healthy subjects and patients with DCM, it is possible to compare both patterns of cardiac deformation within the cardiac cycle in order to analyze the differences between them. Positive strain values describe myocardial thickening and negative values describe its shortening, related to its original length. During myocardial contraction, the radial strain is positive due to myocardial thickening, and the circumferential strain is negative due to myocardial shortening.

The tracking methods were successfully applied on heathy and DCM patients and the tags were successfully detected during systole and diastole. A comparison between the strains, by Mann-Whitney statistical test, during the cardiac cycle in both sets of subjects, identified a significant difference ($p<0.05$) between them. It was observed that in healthy subjects, the radial strain varied from 18.63 % to 43.84 %, while in DCM patients, the radial strain varied from 10.73 % to 14.14 %. The radial strains are positive values, as the LV thickens during myocardial contraction. The results of this thesis are in agreement with previous studies done with DCM and healthy subjects, as the ranges of deformations are similar in both sets of subjects. Moreover, this thesis also confirms that DCM patients have lower radial strain values than healthy subjects, as DCM is characterized by a decrease in heart muscle strain during the cardiac cycle. By comparing several segments in the different sections of the heart, it was also observed that in DCM patients, the minimum deformation was on the inferolateral segment of the base, while the maximum was on the anteroseptal segment of the middle section. However, in healthy subjects, the minimum deformation was on the anterior segment and the maximum was on the inferoseptal segment, both in the middle section of the left ventricle. This result was also observed in previous studies.

Regarding to the circumferential strains analysis, it was observed that in healthy subjects, the average circumferential strain range was from -32.17 % to -24.33 %, while in DCM patients,

it was from -15.92 % to -8.17 %. The negative value of the circumferential strain means that there was a LV wall shortening and this is in conformity with the correct behavior of LV during myocardial contraction. Moreover, in healthy subjects, the mid section of LV has the major strain, while in DCM patients, it is the apical section. A comparison between the circumferential strains during systole in both sets of subjects supports the previous studies results, in which the circumferential stains values are negative during systole. Additionally, the results of Mann-Whitney statistical test also shown significant lower absolute ($p<0.05$) values on DCM patients, when comparing to healthy subjects.

Additionally, the effect of the gender (male/ female) on the strains was also investigated on the DCM patients and the results suggest that in women, the LV strain is lower than in men. Despite these results, the other studies did not report any conclusion related to this effect.

It is possible to state that the study of the LV strain is an important parameter in the evaluation of the cardiac contractility. A non-invasive assessment of LV by MRI and the superimposed grid created by SPAMM improved the tracking of LV wall strains. Another important conclusion of this study was that DCM decreases the deformation capabilities of the heart, as it is responsible for the wall thinning and dilation of heart chambers, causing a decrease in wall radial and circumferential strains. Moreover, it was observed that the major section responsible for the myocardial deformation was the middle section of the LV. Finally, this thesis also confirmed that during myocardial contraction, the radial strain values are positive due to the myocardial thickening and the circumferential values are negative due to the myocardial shortening.

A need to automatically detect the LV and also to efficiently calculate the LV strains in a short time can be developed as a future work, which will also improve the analysis of DCM disease and other cardiac diseases.

Keywords: Cardiac wall deformation; Magnetic Resonance Imaging (MRI); Spatial Modulation of Magnetization (SPAMM); Left ventricle (LV); Dilated cardiomyopathy (DCM)

Resumo

As doenças cardiovasculares são uma das maiores causas de morte no mundo, causando aproximadamente 17.5 milhões de mortes por ano, o que corresponde a 31% de todas as mortes no mundo. Estas doenças caracterizam-se pela diminuição da contração da parede do miocárdio durante o ciclo cardíaco. Uma das doenças mais comuns é a cardiomiopatia dilatada (DCM), onde o músculo cardíaco fica mais fino e fraco, e as cavidades cardíacas ficam aumentadas. Consequentemente, a capacidade de deformação do miocárdio é diminuída, o que impossibilita o coração de bombear eficientemente o sangue para as restantes partes do corpo. Esta condição é maioritariamente genética, mas também pode ser provocada por diferentes causas como infeções virais, inflamações ou lesões.

A análise da deformação da parede do miocárdio aquando do ciclo cardíaco possibilita não só a identificação das deformações normais do miocárdio aquando da sua contração, mas também das deformações anormais devido a doenças cardíacas. A técnica de ressonância magnética cardíaca (CMR) é não invasiva e tem uma elevada resolução espacial, sendo por isso indispensável no estudo destas deformações. Esta técnica permite detetar essas mesmas características da contração e distensão do músculo cardíaco, possibilitando a análise das deformações e a respetiva distinção entre os pacientes saudáveis e os pacientes com cardiomiopatia dilatada. Nesta doença, observa-se o estreitamento das paredes do miocárdio e a dilatação das cavidades cardíacas, como é o caso do ventrículo esquerdo, o que se observa pelo aumento do seu diâmetro. O resultado é um decréscimo significativo na tensão e deformação da parede do miocárdio, o que impacta negativamente na eficiência da sístole ventricular. A técnica de Modulação Espacial da Magnetização (SPAMM) tem vindo a ser proposta para a visualização do movimento e deslocamento da parede do miocárdio no seu plano de imagem, através da criação de padrões de linhas e grelhas com magnetização alterada na imagem. Estes padrões são marcadores que seguem a deformação do músculo cardíaco. Ao serem detetados e seguidos durante o ciclo cardíaco, estes marcadores contribuem para o estudo do movimento da parede do miocárdio aquando da sua contração.

A amostra usada nesta tese consistiu em imagens de ressonância magnética cardíaca de 9 indivíduos, 3 dos quais são saudáveis e os outros 6 são pacientes com DCM. As imagens foram adquiridas pelo Hospital Motol em Praga (República Checa) e analisadas pelo Instituto de Informática, Robótica and Cibernética da Faculdade de Engenharia Elétrica em Praga.

A tese proposta teve como objetivo o estudo da deformação radial no ventrículo esquerdo através da automatização na deteção dos marcadores presentes no mesmo, assim como no seu seguimento ao longo do ciclo cardíaco. Pela análise das deformações de voluntários saudáveis e de pacientes com cardiomiopatia dilatada, é possível comparar os seus padrões de deformação cardíaca de modo a analisar as diferenças entre os dois. Pelo estudo das deformações, sabe-se que um valor positivo de deformação corresponde a um espessamento de um objeto e um valor negativo corresponde ao seu encurtamento, relativamente ao seu tamanho inicial. Durante a contração do miocárdio, é normal observar-se um espessamento e encurtamento da parede do ventrículo esquerdo. Assim sendo, as deformações radiais tomam valores positivos devido ao espessamento da parede e as circunferenciais tomam valores negativos devido ao encurtamento da parede.

Os métodos de deteção dos marcadores foram aplicados com sucesso nos sujeitos

saudáveis e com cardiomiopatia dilatada, sendo que estes marcadores foram também corretamente seguidos ao longo do ciclo cardíaco, durante a sístole e a diástole. Nos sujeitos saudáveis, foi observado um intervalo de deformações radiais entre 18.63 % e 43.84 %, enquanto que em pacientes com cardiomiopatia dilatada, os valores de deformação radial variaram entre 10.73 % e 14.14 %. De notar que os valores das deformações radiais são positivos e, por isso, confirmam o espessamento da parede do ventrículo esquerdo aquando da sua contração. Assim sendo, os resultados desta dissertação vão de encontro com os resultados dos testes feitos anteriormente em voluntários saudáveis e com cardiomiopatia dilatada, visto que os intervalos de deformações são semelhantes para os dois grupos. Ao comparar-se as deformações dos dois grupos pelo teste estatístico Mann-Whitney, verificou-se uma diferença significativa ($p<0.05$) nos valores das deformações entre os mesmos. Assim sendo, esta tese também confirma que os pacientes com a doença cardíaca têm valores mais baixos de deformação em relação aos indivíduos saudáveis, tal como é comprovado pelo facto da doença cardiomiopatia dilatada ser caracterizada pela diminuição da deformação do miocárdio durante o ciclo cardíaco.

Pela comparação dos diferentes segmentos ao longo das secções básica, média e apical do ventrículo esquerdo, foi também observado que nos pacientes com cardiomiopatia dilatada, a deformação mínima correspondeu ao segmento inferolateral da base do ventrículo e que a deformação máxima se deu no segmento anteroseptal da secção media do ventrículo. Em contrapartida, nos indivíduos saudáveis, o mínimo da deformação foi no segmento anterior e o máximo da deformação correspondeu ao segmento inferoseptal, ambos os segmentos pertencentes à secção media do ventrículo esquerdo. Estes resultados foram também observados em estudos anteriores relativos a pacientes com cardiomiopatia dilatada.

Relativamente à análise das deformações circunferenciais, foi observado que, nos sujeitos saudáveis, o intervalo das deformações esteve entre -32.17 % e -24.33 %, enquanto que nos pacientes com cardiomiopatia dilatada, o intervalo foi de -15.92 % a -8.17 %. O valor negativo da deformação circunferencial é devido ao encurtamento da parede do ventrículo esquerdo, sendo que este valor se encontra em conformidade com o correto comportamento da parede do ventrículo durante a contração do miocárdio, tal como observado em estudos anteriores. Para alem destes factos, também se verificou que o máximo da deformação circunferencial foi dado na secção media do ventrículo esquerdo, enquanto que o mínimo foi na secção apical do mesmo. Ao comparar-se as deformações circunferenciais, pelo teste estatístico Mann-Whitney, durante a systole e entre os dois grupos de sujeitos, verificou-se existe uma diminuição significativa ($p<0.05$) do seu valor absoluto nos pacientes, relativamente aos sujeitos saudáveis.

Adicionalmente, também foi estudado o efeito do género (masculino / feminino) nas deformações dos pacientes com cardiomiopatia dilatada. Os resultados do estudo mostraram que as deformações do ventrículo esquerdo são maiores no género masculino, em relação ao género feminino. Contudo, outros estudos realizados anteriormente não relataram qualquer relação entre as deformações do miocárdio e o género (masculino / feminino) dos respetivos pacientes.

Com esta dissertação foi possível concluir que o estudo das deformações no ventrículo esquerdo é um parâmetro importante na avaliação da contratilidade do coração. O facto de a Ressonância magnética ser uma técnica não invasiva e da técnica de Modulação espacial da magnetização permitir criar um padrão de grelha que facilmente acompanha movimentos na parede do músculo, possibilitou a eficiente deteção das deformações na parede do ventrículo esquerdo. Uma outra conclusão importante deste estudo é o facto da doença cardiomiopatia dilatada provocar uma diminuição da capacidade de deformação do coração, visto que a doença é caracterizada pelo estreitamento da parede do miocardio e por uma dilatação das cavidades cardíacas, especialmente dos ventrículos. Este facto está na origem da diminuição das

deformações radiais e circunferenciais, em relação às deformações dos pacientes saudáveis.

Foi também observado que a secção do ventrículo esquerdo responsável pela maior deformação é a secção média, pois foi nesta secção que se observou um maior número de valores máximos de deformação.

Por fim, nesta tese também se confirma que durante a contração do miocárdio, a deformação radial teve valores positivos e a deformação circunferencial teve valores negativos, o que comprova que houve um espessamento e encurtamento da parede do ventrículo esquerdo durante a sua contração.

Assim sendo, verifica-se que ao longo desta dissertação foi possível analisar a relação da deformação do ventrículo esquerdo com a doença cardiomiopatia dilatada e consequentemente, avaliar se a deformação calculada é normal ou devido à doença cardíaca. Como tal, a partir deste estudo foi possível facilitar a deteção das deformações, bem como fazer a sua análise para contribuição do estudo das doenças cardíacas, tal como a cardiomiopatia dilatada.

Como trabalho futuro, poderá estudar-se como detetar automaticamente o ventrículo esquerdo e como calcular eficientemente as suas deformações. Assim, poderá também aprofundar-se o estudo e a análise da doença cardiomiopatia dilatada e de outras doenças cardíacas.

Palavras-chave: Deformação da parede cardíaca; Ressonância magnética (MRI); Modulação Espacial da Magnetização (SPAMM); Ventrículo Esquerdo (LV); Cardiomiopatia Dilatada (DCM)

Contents

List of Figures

List of Tables

List of Abbreviations

AV - Atrioventricular

CAD- Coronary artery disease

CVD - Cardiovascular disease

CRT - Cardiac resynchronization therapy

CMR - Cardiovascular magnetic resonance

CT - Computed tomography

DCM - Dilated cardiomyopathy

EBCT - Electron-beam computed tomography

ECG - Electrocardiogram

FID - Free Induction Decay

FT - Fourier transform

GE - Gradient Echo

HARP - Harmonic phase

LA - Left Atrium

LV - Left Ventricle

MRI - Magnetic resonance imaging

MDCT - Multi-detector computed tomography

NMR - Nuclear magnetic resonance

NMV - Net magnetic vector

PET - Positron emission tomography

RA - Right Atrium

RF - Radio-frequency

ROI - Region of Interest

RV - Right Ventricle

SNR - Signal-to-noise ratio

SA - Short-axis

SE - Spin Echo

SPAMM - Spatial modulation of magnetization

SPECT - Single photon emission computed tomography

SSFP - Steady State Free Precession

TE - Echo time

TR - Repetition Time

1D - One Dimensional

2D - Two Dimensional

3D - Three Dimensional

1. Introduction

1.1 Introduction / Aim

According to the *World Health Organization*, cardiovascular diseases (CVD) cause approximately 17.5 million deaths per year, which corresponds to 31% of all deaths worldwide. Additionally, more than 75% of CVD deaths occur in low-income and middle-income countries and four out of five CVD deaths are caused by heart attacks and strokes [1]. In Europe, CVD causes 47% of all deaths each year, which corresponds to 4 million deaths [2]. Therefore, it is considered one of the main causes of death in the western world as it causes considerable morbidity and mortality.

Magnetic Resonance Imaging (MRI) has been indispensable for studying these diseases because it is a non-invasive technique with excellent spatial resolution [3]. Moreover, an important MRI technique, the spatial modulation of magnetization (SPAMM), was used to study not only a specific tissue characteristic, but also its strain capability. This technique is based on tagged MR imaging, which means a grid is superimposed to the image to track the tissue motion. The deformation of the grid will automatically allow tissue strain detection and respective quantification.

Since the left ventricle (LV) controls systemic perfusion and ensures the oxygenation and nutrition supply of the entire body, then the left ventricular contractile function is the main representative of overall cardiac performance [4]. For that reason, the tissue studied in this thesis is the LV wall and there is also a need to analyze how the LV strain is related to the cardiovascular diseases, in specific to dilated cardiomyopathy (DCM), which will be later explained in detail.

1.2 Motivation and Goals

The main goal of this project was the development of an automatic algorithm to detect and track the left ventricle wall displacement and strains in sequences of tagged MR images during the cardiac cycle. The detection and respective evaluation of the wall deformation enables to correctly evaluate if it is normal or pathological due to a cardiovascular or heart disease. Therefore, the algorithm development and implementation could have a significant impact on the patient diagnosis and pathology evaluation, as the results of this project can make it easier and more efficient to distinguish strains measured on healthy subjects and DCM patients.

The second aim was to apply these detection methods to healthy subjects and DCM patients. The goal is to evaluate its potential to provide clinical decision support to medical professionals as doctors, specially cardiologists, and also to medical physicists and researchers, by contributing to the progress of the current state of knowledge on cardiac MRI topic.

1.3 Structure of the dissertation

This thesis is structured as follows:

Chapter 2 explores and explains the supporting concepts of this work, particularly the human heart anatomy, physiology and types of motion strains. It also reviews the state-of-the-art of cardiac imaging techniques, especially cardiac MRI, focusing on SPAMM.

Chapter 3 describes the proposed method for automatic detection and tracking of the left ventricle wall grid displacement and deformation in SPAMM cardiac MR images, obtained from a data set of eleven subjects.

Chapter 4 presents the set of results, consisting of visualization of the LV wall displacement and deformation during systole and diastole in the base, middle and apical parts of LV. LV radial and circumferential strains of healthy subjects and DCM patients and the comparison between both are presented as well.

Chapter 5 analyses the results obtained and presents a set of conclusions of this dissertation, main contributions and their importance on further research and application in clinical routine.

2. Supporting concepts and background

2.1 Human heart

As one of the vital organs, the heart was long identified as the center of the entire body and the seat of life. In the fourth century, Aristotle identified the heart as the most important organ of the body [5]. Given that the heart quickens its pace when people are emotionally aroused, he thought it served primarily as the seat of emotion but also that it might also be a source of heat. In the sixteenth century, dissections and anatomical charts of Vesalius greatly improved knowledge of cardiovascular anatomy and set the stage for a more scientific study of the heart and treatment of its disorders [6]. In the last several decades, such advances as coronary bypass surgery, replacement of diseased valves, heart transplants, artificial pacemakers, and artificial hearts have made cardiology one of the most attention-getting fields of medicine [6].

2.1.1 Anatomy

The cardiovascular system consists of the heart, blood vessels and approximately 5 liters of blood transported by the blood vessels [7].

The heart is located inside the thoracic cavity in the mediastinum and is bordered bilaterally by the lungs, anteriorly by the sternum and inferiorly by the diaphragm (Figure 2.1). The base is the broad superior portion of the heart and the point of attachment for the great vessels, and the inferior end is the apex of the heart. From the base to the apex, it is slightly tilted towards the left and about two-thirds of the heart lies to the left side of the median plane. The heart is enclosed in a double walled sac called the pericardium, which is the anchor of the great vessels. It is not only responsible for protecting the heart from infection, but also for keeping the heart contained in the chest cavity and not over-expanding when blood volume increases. Between the two pericardium walls, there is a small amount of fluid that serves as a lubricant and a shock absorber of the heart [6].

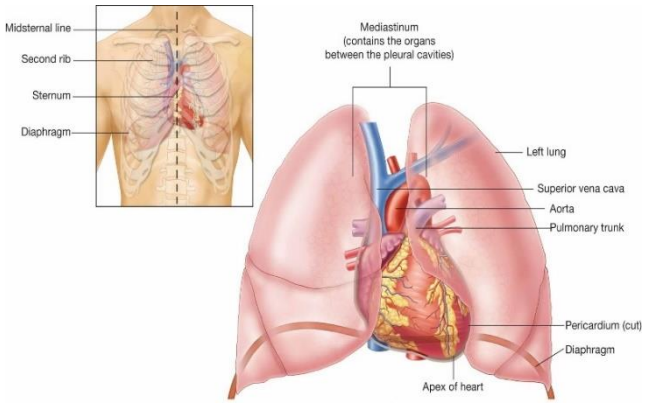

Figure 2.1: Location of the heart inside the thoracic cavity (left) and the spatial relation between the heart and lungs (right). Adapted from [8].

The heart consists of three layers: a thin epicardium covering its external surface, a thick muscular myocardium in the middle, and a thin endocardium lining the interior of the chambers [9]. The epicardium is a serous membrane on the heart surface. In some places, it also includes a thick layer of adipose tissue, whereas in other areas it is fat free and translucent, so the muscle of the underlying myocardium is shown through. The endocardium lines the interior of the heart chambers, covers the valve surfaces and is contiguous with the endothelium of the blood vessels. The myocardium forms a thick layer between the outer epicardium layer and the inner endocardium layer. The thickness of this cardiac muscle is proportional to the workload on the heart chambers.

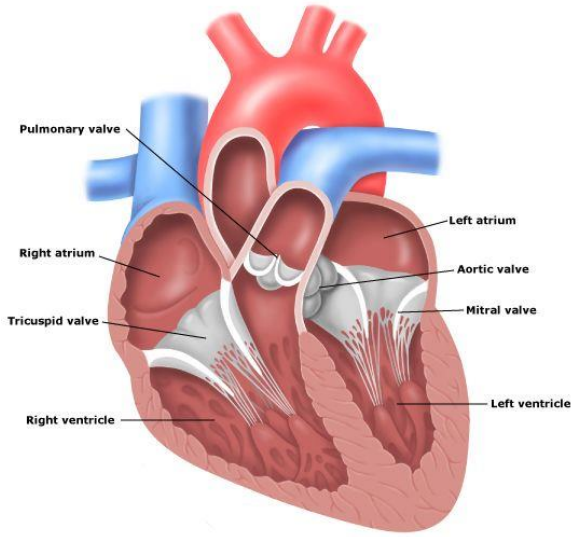

Figure 2.2: Cardiac chambers (right atrium, right ventricle, left atrium and left ventricle) and valves (tricuspid and mitral). Adapted from [10].

The interior of the heart is divided into four cavities (Figure 2.2): right atrium (RA), left atrium (LA), right ventricle (RV) and left ventricle (LV). The RA and RV are separated from the LA and LV by the interatrial and interventricular septum respectively.

The unidirectional blood flow is ensured by the cardiac valves: the atrioventricular (AV) valves prevent the reflux of blood from the ventricles back to the atria and the semilunar valves prevent the reflux of blood from the main arterial trunks back to the ventricles. The right AV valve is designated by tricuspid valve and the left AV valve by bicuspid (or mitral) valve. The right semilunar valve is designated by pulmonary valve and the left semilunar valve by aortic valve. These valves obstruct the passage of blood when it starts flowing back to the ventricles during ventricular relaxation.

Because this thesis is focused in LV strains, it is essential to understand the anatomy of this structure. Morphologically, the LV in a normal heart is a thick-walled chamber that forms the apex and the lower part of the left and posterior heart border. Externally, the LV is shaped like a cone. Internally, it is demarcated by its fine and numerous trabeculations and an inlet and outlet portion. The inlet component contains the mitral valve and extends to the attachments of the prominent papillary muscles. These papillary muscles exist on the inner surface of the ventricles and are attached by the *chordae tendineae* to the mitral valve, in order to prevent it from prolapsing during the ventricular contraction. The outlet part consists of the aortic valve and is in direct continuity with the inlet part.

The heart has also a connective tissue meshwork of collagenous and elastic fibers called the fibrous skeleton. One of its multiple functions is to provide structural support to the heart, especially around the valves and the attachments to the great vessels. Another function is to hold these orifices open and prevent them from being excessively stretched when blood surges through them. As a nonconductor of electricity, it also serves as electrical insulation between the atria and the ventricles, so that the atria cannot stimulate the ventricles directly.

2.1.2 Physiology

The cardiovascular system (Figure 2.3) is responsible for the transportation of oxygen, nutrients, hormones and cellular waste products within the human body [7]. The heart is a muscular pump that powers the cardiovascular system and keeps blood flowing through circulatory system vessels.

The right side of the heart is involved in the pulmonary circuit. The deoxygenated blood from the body tissues (from the upper and lower body via the superior and inferior vena cava, respectively) is received by the RA. Then, it passes through the tricuspid valve into the RV and it is pumped to the lungs via the pulmonary artery, where carbon dioxide is released, and oxygen is captured. The oxygenated blood then returns to the left side of the heart, which is involved in the systemic circuit. The blood is received by the LA via the pulmonary veins and passes through the bicuspid valve into the left ventricle. Then, it is pumped to the aorta under high pressure to ensure that the oxygenated blood reaches all the body tissues effectively, in order to deliver oxygen and pick up carbon dioxide and other wastes. After exchanging gases with the tissues, the deoxygenated blood returns to the RA for another cycle and so on.

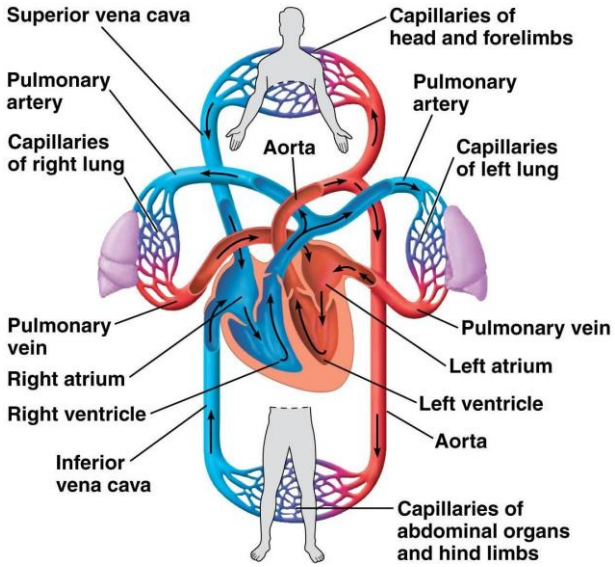

Figure 2.3: The circulatory system. The oxygenated blood is represented in red and the deoxygenated blood is shown in blue. The circulation of blood between the heart and lungs represents the pulmonary circuit and the systemic circuit is represented by the blood flow from the heart and the body tissues. Adapted from [11].

2.1.3 Cardiac cycle

Cardiac cycle is the sequence of events that begins with contraction of the atria and ends with the relaxation of ventricles. The mechanical events are coordinated by the electrical activity of the heart, which is recorded by the Electrocardiogram (ECG) [12] (Figure 2.4).

The period of relaxation that occurs as the blood passively fills the chambers is denominated diastole. The period of contraction that the atria undergo while blood is pumped into the ventricles is named atrial systole. The ventricular systole takes place when the ventricles contract to pump blood into the blood vessels. As both atria and ventricles go through diastole and systole, it is essential that these processes are carefully regulated and coordinated to ensure blood is pumped efficiently to the body [13].

During diastole, blood flows passively from the atria into the ventricles as the AV valves are opened and the semilunar ones are closed. The ventricles are filled up to approximately 70-80 percent of their capacity [13]. The pressure inside the atria rises until an electrical stimulus denominated action potential triggers the atria to contract. Then, blood is pumped into the ventricles and fills the remaining 20-30 % of their volume. This phase is the atrial systole and is represented by the P wave of the ECG.

While the atrial pressure diminishes to its baseline, the ventricle pressure starts to rise until its maximum. The ventricular systole happens when blood is pumped, through the semilunar valves from the RV, and into the aorta from the left ventricle. This phase is represented by the QRS complex in the ECG.

As the pressure inside the ventricles starts to reduce to its baseline, the semilunar valves close and the AV valves open again. The ventricular relaxation is represented by the T wave in ECG. At this point, a new cardiac cycle starts and begins with diastole, as previously described.

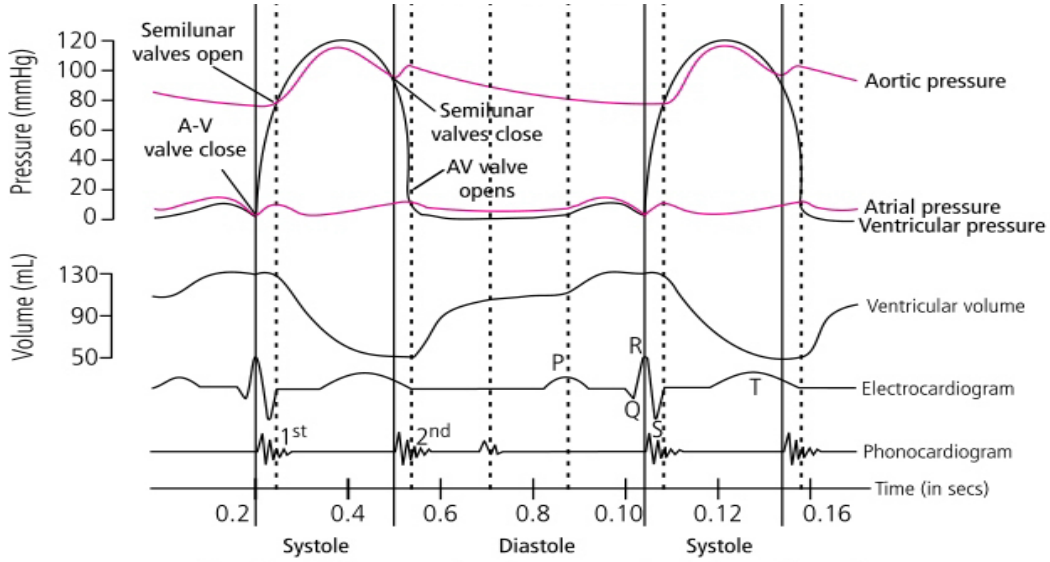

Figure 2.4: Different events during the cardiac cycle and their representation in ECG. The top three curves show the pressure changes in the aorta, left ventricle, and left atrium, respectively. The P wave represents depolarization of the atria and is followed by atrial systole. The QRS complex represents depolarization of the ventricles and is followed by ventricular contraction. At this point, the atria relax. The T wave represents the repolarization of the ventricles and marks the beginning of ventricular relaxation. Adapted from [13].

2.1.4 The electrical conduction system

Cardiac myocytes are auto-rhythmic because they electrically depolarize at regular time intervals. Some of the myocytes lose their ability to contract and become specialized for generating and conducting these electrical signals, instead. These cells constitute the cardiac conduction system (Figure 2.5), which controls the route and timing of stimulation to ensure that the four heart chambers are coordinated with each other [13].

Being able to create its own electrical impulses and control them via a specialized conduction pathway, makes the heart a natural pacemaker.

The electrical signal arises from a spontaneous generated action potential in the sinoatrial (SA) node, which is a patch of modified myocytes in the RA, just under the epicardium and near the superior vena cava. It is also named as natural pacemaker since it initiates each heartbeat [13].

Each stimulus passes through the myocardial cells of the atria creating a wave of contraction to the AV node. The latter is a similar patch of modified myocytes located at the lower end of the atrial septum, near the right AV valve, and acts as an electrical gateway to the ventricles. All electrical signals traveling to the ventricles must pass through the AV node because the fibrous skeleton acts as an insulator that prevents currents from traveling to the ventricles by any other route. By reaching the AV node, the electrical stimulus from the SA node is briefly delayed so that the atria can contract ahead of the ventricle contraction, thereby pumping blood into the ventricles before they contract. Once the atria are empty, the AV valves between the atria and ventricles close. The atria begin to refill and the electrical stimulus passes through the AV node into the bundle of His and Purkinje fibers, which causes the ventricular contraction [13].

At this point the ventricles are empty, the atria are full and the valves between them are closed. The SA node is about to release another electrical stimulus and the process is about to repeat itself. This process takes less than one third of a second [6].

The bundle of His is a cord of modified myocytes leaving the AV node and traveling to the interventricular septum. It splits into right and left bundle branches, enters the septum and descends toward the apex of the heart.

The specialized and conducting Purkinje fibers arise from the lower end of the bundle branches and propagate the electrical excitation to the ventricular myocytes, causing the ventricles to contract and to generate force to eject blood out of the heart.

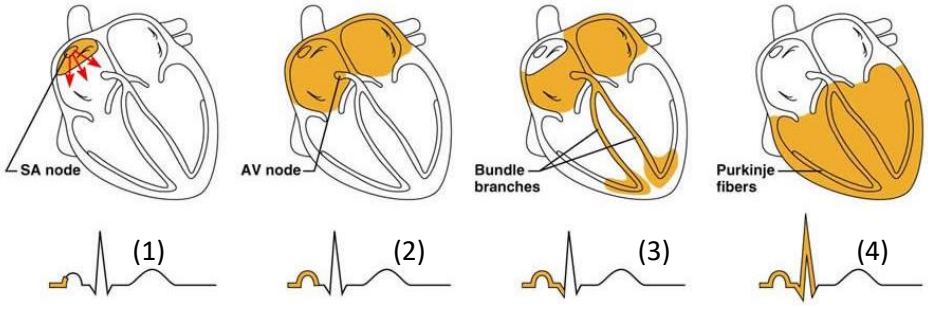

Figure 2.5: The SA node generates the electrical signal (1), which is delayed in AV node (2). This leads to the atrial contraction. The signal then passes through the bundle branches (3) to the Purkinje fibers (4), which causes the ventricular contraction. Adapted from [14].

2.1.5 Cardiovascular Diseases

CVD are a group of heart and blood vessel disorders [15]. Blood vessels disorders consist of a narrowing of the blood vessels causing the restriction in blood supply to the heart (coronary disease), which can lead to a heart attack, and to the arteries in body peripheries as legs and feet (peripheral vascular disease). The main cause of blood vessels disorders is atherosclerosis, in which the fatty deposits build up in the inner walls of these arteries to form plaques and affecting blood circulation.

Regarding heart disorders, the main categories include hypertensive heart disease, inflammatory heart disease, heart failure and cardiomyopathy [16].

Hypertensive heart disease [15] occurs when high blood pressure is severe or prolonged enough to cause damage in the heart or blood vessels. The excess pressure required to pump blood through the blood vessels makes it difficult for the heart to work, leading to its thickening and enlargement. This usually happens in the main pumping chamber of the heart, the left ventricle, and the condition is known as left ventricular hypertrophy.

Inflammatory heart disease [16] is usually caused by a viral infection and can be an inflammation of heart muscle (myocarditis), the pericardium sac (pericarditis) and the inner layer of the heart wall (endocarditis). Rheumatic heart disease is an example of inflammatory heart disease, in which the heart and the valves are damaged due to one or more rheumatic fever attacks, usually occurred in childhood. In some cases, the infection may result in scarring of the valves, weakening of the heart muscle, or damage to the pericardium sac. If the valves are scarred, they do not open and close normally, and consequently the blood circulation will be affected.

Heart failure (HF) [17] can be the result of all forms of cardiac disease that impair and overload the heart. It occurs when the heart becomes too damaged to effectively pump blood through the body, preventing the organs from getting enough blood and oxygen. Although it can occur suddenly, it is usually developed during several years, as the heart gradually becomes weaker and works less effectively.

Cardiomyopathies [15] [16] are a group of conditions in which the direct and widespread damage to the heart muscle makes it weaker. The condition can be genetic or due to various causes such as viral infections, inflammation or injuries. One of the most common types of cardiomyopathies is dilated cardiomyopathy (DCM), in which the heart is enlarged. Other types include ischemic, where there is a loss of heart muscle, and also hypertrophic cardiomyopathy, in which the heart muscle is thickened.

Since this thesis analyses strains from healthy subjects and patients with DCM, this type of CVD is next explained in detail. DCM is a condition in which the heart becomes enlarged and cannot pump blood efficiently. It is characterized by the presence of a thin myocardium wall, decreased number of myocytes and also fibrosis.

At least 25% of individuals in Western populations have evidence of genetic DCM with predominantly autosomal dominant inheritance [18]. Family history of premature cardiac death or conduction system disease can also be related to genetic causes. Acquired causes of DCM can also exist and include nutritional deficiencies, endocrine dysfunction, and administration of toxic drugs [18]. Additionally, this disease can also occur at a late stage following cardiac infection and inflammation. In contrast to active myocarditis, which is an acute inflammatory heart disorder with often preserved left ventricular size, inflammatory DCM is defined by the presence of chronic inflammatory cells with LV dilatation and reduced ejection fraction [19].

Cardiac MRI is able to characterize cardiomyopathies by their morphologic and functional phenotype as well as by tissue characterization, which is based on the relaxation parameters of MRI such as T1 and T2 that will be explained in section 2.3. Long T1 and T2 can denote the presence of an increased water content inside the myocardial tissue, as a result of an edema (from acute infarction or myocarditis), and the presence of dilated cardiomyopathies as well. The characteristic abnormalities of DCM seen on MRI are reduced wall thickening, dilation of heart chambers, and impaired myocardial fiber shortening. The increase in chamber size in combination with thinned myocardial walls is due to myocyte apoptosis and elongation [20]. This causes a typical eccentric ventricular hypertrophy with a decreased wall thickness, thereby increasing the diameter of the ventricle (Figure 2.6). The net result is a significant decrease in wall stress and strain, which has a negative impact on systolic ventricular performance.

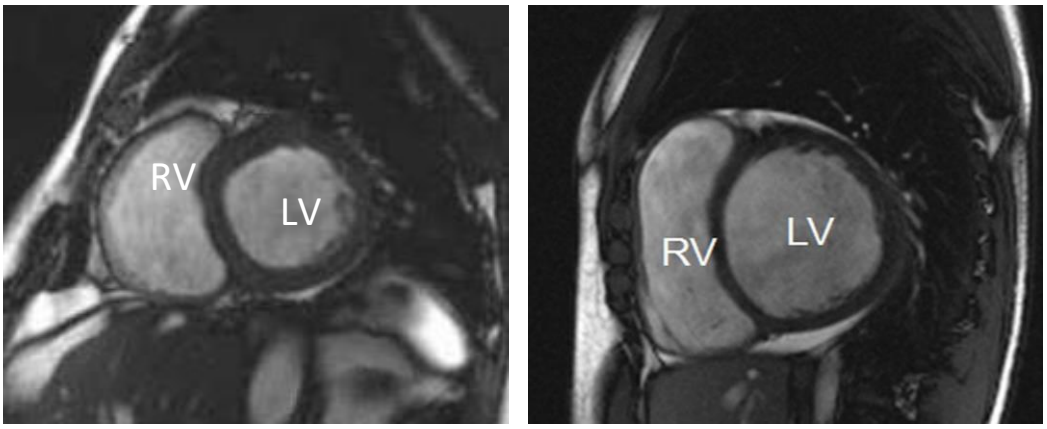

Figure 2.6: Representative short axis MRI of a healthy patient (left) and a patient with DCM (right). The DCM patient has a dilated LV and a thinner LV wall in comparison to the healthy patient, who has a non-dilated LV and an LV wall with normal thickness. Adapted from [21][22].

The implementation of cardiac resynchronization therapy (CRT) has been shown to improve the general quality of life and survival rates in patients with DCM and HF. In this therapy, a biventricular pacemaker is placed to activate both septal and lateral walls of the LV. By pacing both sides of the left ventricle, the pacemaker can resynchronize a heart whose opposing walls were not contracting in synchrony. MRI provides strategies to identify the patients' response to CRT by analysing wall motion, regional myocardial thickening and differences in maximal wall thickening timing in cine-MRI images. Additionally, MRI can provide useful information in pre-CRT imaging by visualizing regional dyssynchrony itself.

Most cardiovascular diseases are caused by behavioural risk factors such as harmful use of alcohol or tobacco, unhealthy diet and obesity, physical inactivity, and also hypertension, diabetes and hyperlipidemia. Besides adopting a healthy lifestyle, the best way to reverse this reality is to be able to perform an early and efficient diagnosis of the CVD. For the early diagnosis of anomalous contraction, it is important to assess and analyze regional myocardial displacement and deformation in order to ensure that those in need receive appropriate treatment and therapy. Therefore, the development of accurate diagnostic tools such as MRI is necessary to achieve good results when it comes to measure parameters to describe patient's pathology. The greatest virtue

of MRI is to evaluate several different relevant markers as ventricular volumes, mass and function in one single exam, since these parameters are major determinants of therapy response and prognosis. This imaging technique along with systematic analysis ensures highly reproducible measurements, and can be considered as the standard reference for quantification of LV and RV volumes and function [23]. Furthermore, strain imaging offers the opportunity to quantify both magnitude and timing of regional systolic and diastolic deformation. Given its spatial resolution, strain MRI has been particularly useful in detecting regional myocardial dysfunction related to cardiomyopathies, ischemia, fibrosis and other cardiovascular diseases [24].

2.2 Cardiac imaging

Cardiac imaging is used to diagnose and identify various forms of heart disease, establishing the risk of developing future heart diseases, and to decide on the necessity for additional medical treatments and procedures [25].

2.2.1 Radiography

Radiography is the process of photographing internal structures with X-rays. Until 1960, this was the only imaging method that was widely available. X-rays are absorbed by dense tissues such as bones, teeth and tumors, which leave the image lighter in these areas. Chest X-rays (Figure 2.7) are often useful as a starting point in a cardiac diagnosis. Changes in heart's size and shape may, for example, indicate heart failure or heart valve problems. Additionally, chest X-rays can indicate the presence of calcium within the heart or blood vessels, which may indicate damage in heart valves, coronary arteries or heart muscle [26].

Although posterior, anterior and lateral X-rays views provide a gross view of atrial and ventricular size and shape, additional tests are almost always required for precise characterization of cardiac structure and function. Some other disadvantages of radiography are that images of overlapping organs can be confusing and slight differences in tissue density are not easily detected. In addition, X-rays are a type of ionizing radiation and therefore cannot be used indiscriminately.

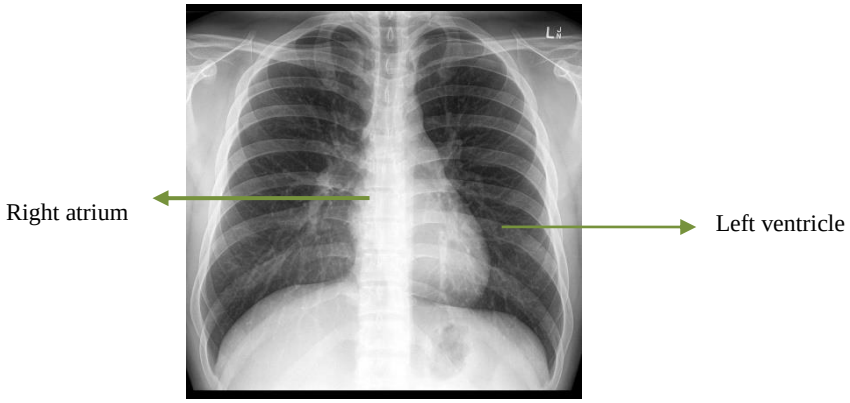

Figure 2.7: Chest X-ray. Adapted from [27].

2.2.2 Computed Tomography

Computed tomography (CT) is a more sophisticated application of X-rays developed in 1972. The patient is moved through a ring-shaped machine that emits low-intensity X-rays on one side and receives them in a detector on the opposite side. A computer analyzes signals from the detector and produces an image of a thin "slice" of the body and a series of these images construct a three-dimensional image of the body. Cardiac CT (Figure 2.8) obtains the images of the heart and blood vessels and can help in the detection of coronary disease or problems with the valves and heart function.

Modern CT scanners such as an electron-beam (EBCT) or a multidetector (MDCT) CT are very fast and accurate. The first type of scanner allows the detection of coronary atherosclerosis by showing calcium and cholesterol deposit blockages in coronary arteries. The second one images the heart's structure and a scarred myocardium caused by a possible heart attack. It is also capable of detecting the fluid inside the pericardial sac and any abnormalities in the large blood vessels of the heart [28].

CT scanning has the advantage of imaging thin sections of the body, so there is less organ overlap and the image is much sharper than in a conventional X-ray. CT scanning is also useful for identifying tumors and aneurysms and has replaced most exploratory surgery. However, it requires extensive knowledge of cross-sectional anatomy to interpret the images and caution with the cumulative number of X-ray examinations and/or treatments over a long period of time.

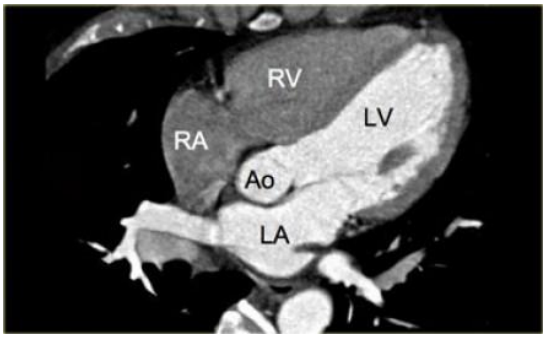

Figure 2.8: Cardiac CT. Right Atrium (RA), Right Ventricle (RV), Aorta, Left Atrium (LA), Left Ventricle (LV). Adapted from [29].

2.2.3 Cardiac Nuclear Imaging

Cardiac nuclear medicine imaging uses radiotracers, which incorporate radioactive isotopes with short half-life, for example carbon-11, into metabolic active molecules like glucose or water, typically injected into the bloodstream, inhaled or swallowed. The radiotracer travels through the heart and gives off energy in the form of gamma rays. Using either a SPECT (single photon emission computed tomography) scanner or PET (positron emission tomography), the

radioactive signal from the heart is detected and produces a detailed three-dimensional image. These techniques can determine the amount of blood flow (perfusion) the heart is receiving, whether the heart cells are functional and healthy (viability), and if the heart has suffered permanent damage from a prior heart attack. They may also be used to help determine whether the heart has been damaged by chemotherapy or radiotherapy and to evaluate the presence of coronary artery disease and cardiomyopathies.

SPECT and PET (Figure 2.9) are used to assess the metabolic state of a tissue and to distinguish which tissues are most active at a given moment. In PET, the procedure begins with an injection of radioactive tracers, which emit positrons. When a positron and electron meet, they annihilate each other and give off gamma rays that can be detected by a gamma detector and analyzed by computer. In contrast with PET, the tracers used in SPECT emit gamma radiation that is measured directly. The result is a series of thin slices covering the whole heart and can be produced from different directions and angles. Computer graphics can be used to create a 3D image of the heart from the thin-sliced images. Different colors or degrees of brightness on the image scan show different levels of tissue function depending on the amount of radioactive tracer used. Therefore, as damaged tissue consumes little or no glucose, it appears dark in the scan.

Cardiologists use cardiac PET and SPECT scans to analyze coronary blood flow, heart damage due to a heart attack, myocardial oxygen consumption and contractile function. Recently, CT scans have been combined with SPECT and PET systems, providing the combination of anatomical imaging from CT with the functional imaging from SPECT or PET. An application in cardiology is the diagnosis of coronary artery disease (CAD).

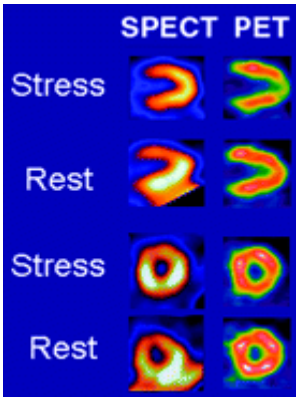

Figure 2.9: Cardiac SPECT and PET images showing the blood flow pattern in the myocardium at rest and stress. Adapted from [31].

2.2.4 Echocardiography

Echocardiography [32] (Figure 2.10) shows the motion and anatomy of the heart in real time. It is the sonographic examination of the heart and has become routinely used in cardiography as it provides information about the size and the shape of the heart, its pumping capacity, and the location and extent of any damage in heart tissues. It is especially useful for assessing valvular and ventricular hemodynamics, and global or regional systolic and diastolic functions. A handheld

device placed tightly to the skin produces high-frequency ultrasound waves and receives the signals reflected from internal organs.

Despite not producing a very sharp image and being highly dependent on operator expertise, the main advantages of echocardiography are its non-invasiveness and the use of inexpensive and portable equipment.

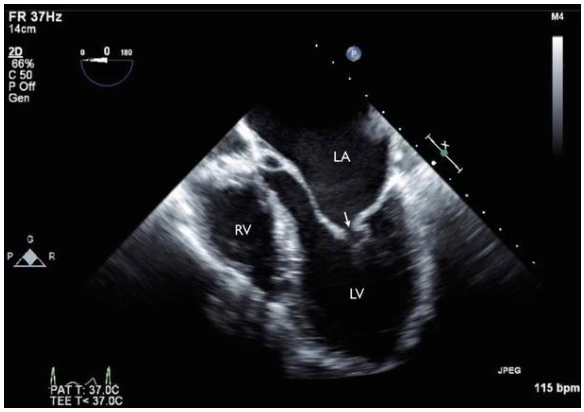

Figure 2.10: Echocardiography imaging of the heart and chambers. Left atrium (LA), Left Ventricle (LV), Right Ventricle (RV). Adapted from [33].

Conventional imaging techniques show only the inner or outer surfaces of the heart as well as the wall thickness and are limited to assessing the motion of the heart wall. Although cardiac function can be evaluated using echocardiography, this technique makes simple geometric assumptions, which are not applicable in distorted heart anatomy. Additionally, the use of CT or X-rays is limited due to the high-energy radiation dose that restricts repeated studies or studies on healthy volunteers. For this reason, among the different available imaging modalities, MRI has become the preferred one to assess cardiac function because of its noninvasiveness and the accuracy and reproducibility of the measurements.

2.3 MRI principles and physics

MRI is a noninvasive imaging technique based in nuclear magnetic resonance (NMR) principles, which deals with atoms with nuclear spin, radio frequency (RF) energy and a strong magnetic field, rather than ionizing radiation used in X-rays or CT.

The magnetic field strength is measured in Tesla (T) and the majority of MRI systems in clinical practice are 1.5 T or 3 T [34]. Typically, MR imaging relies on the magnetic proprieties of nuclei with an odd total number of protons and neutrons, such as the hydrogen nuclei, most of which are located in the water molecules of the body. Each nucleus of hydrogen atom has only one proton, which is a spinning charged particle responsible for producing a magnetic field, according to the classic description of MRI.

2.3.1 Larmor frequency

When a patient is placed in a strong magnetic field B_0, such as an MRI scanner magnetic field of 1.5 T or 3 T, the spinning particles begin to oscillate in a circular motion around B_0 (Figure 2.11). This event is called precession and the frequency of precession (ω_0) is proportional to the strength of B_0, as given by the Larmor frequency equation:

$$\omega_0 = \gamma B_0 \text{ (MHz)} \tag{2.1}$$

where γ is the gyro-magnetic ratio, which is the ratio of the magnetic moment to the intrinsic angular momentum of a spinning particle, such as the hydrogen nucleus spin. At 1 T field, the frequency of precession of the hydrogen atom is 42.58 MHz, so the gyro-magnetic ratio is 42.58 MHz T^{-1} [35].

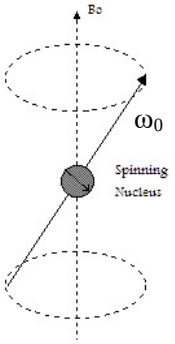

Figure 2.11: Precession of a spin with frequency ω_0 when a magnetic field B_0 is applied. The circle represents the spin and the arrow represents the direction of its magnetization vector. Adapted from [36].

2.3.3 Magnetization and Net magnetic vector (NMV)

Under normal circumstances, the spins are randomly orientated (Figure 2.12-a). The net magnetization vector (NMV) is the sum of all the magnetic moments of the individual spins, and in this case it adds up to be zero. However, when placed in a strong magnetic field like B_0 (Figure 2.12-b), the axes of precession of the spins align either with or against the orientation of the magnetic field accordingly to their energy state. The majority of the spins align parallel to the magnetic field because they are in a low energy state, and the rest align anti-parallel to it, as they are in a high energy state. Consequently, the NMV is aligned with the main magnetic field B_0 in a longitudinal direction, leading to a longitudinal magnetization.

When a RF pulse is applied to the spins with the Larmor frequency (Figure 2.12-c), the spins absorb that energy by resonance. Additionally, they become synchronized and spin together. However, protons that are spinning at different frequencies from the RF pulse frequency do not capture that energy.

The energy from the RF pulse makes the spins flip to a higher energy state, with precession axis opposite to B_0, which forces the magnetization direction to stay in the longitudinal axis but opposite to B_0 direction. If the RF pulse has energy to flip half of the spins to an opposite direction of B_0, it means that half of the spins will be aligned to B_0 and the other half will be aligned to the opposite direction. Therefore, the NMV is oriented perpendicularly to the longitudinal direction. As it turns towards a transverse plane perpendicular to B_0, this is called transverse magnetization.

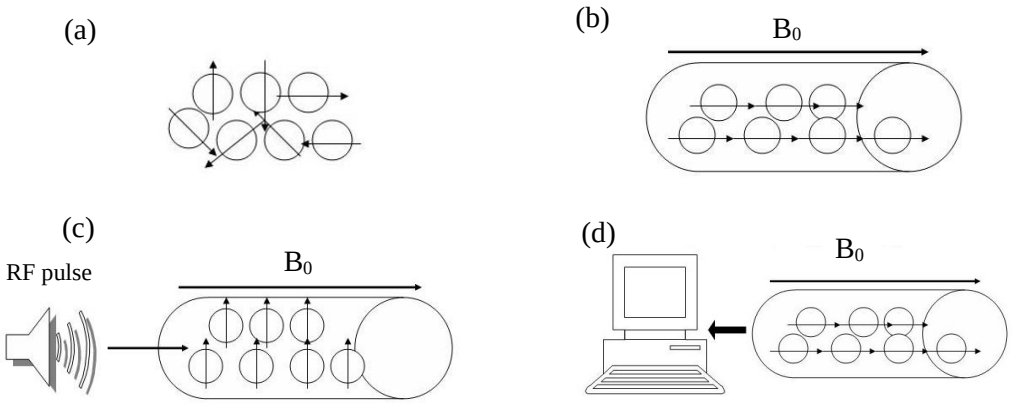

Figure 2.12: (a) Randomly oriented spins when no magnetic field is applied. The circles represent spins and the arrows represent the respective directions of the magnetization vectors. (b) Spins oriented in the direction of the applied magnetic field B_0. The large arrow on top represents the direction of the magnetic field B_0. (c) A RF pulse is applied, which causes the magnetization vectors of the spins to change its direction. (d) RF signal from free induction decay (FID) is received by a computer and processed to construct an MR image from the body part imaged. Adapted from [40].

2.3.4 Relaxation and time constants

When the RF pulse stops, the selected spins relax, i.e. they return to their original alignment with the static magnetic field [40]. The relaxation in the longitudinal axis is governed by the T1 relaxation constant and the relaxation in the transverse axis by the T2 time constant [37]. The T1 relaxation happens when, by giving energy to their surrounding tissues, the spins flip back to their equilibrium energy state and the longitudinal magnetization is recovered. The T2 relaxation happens when the protons that were synchronized and in phase begin to dephase due to the interactions between the spins. Additionally, the time parameter T2* encompasses not only the interactions between the spins, but also the inhomogeneities in the main magnetic field. Those may be the result of intrinsic defects in the magnet itself or from susceptibility-induced field distortions produced by the tissue or other materials placed within the field. Due to T2 and T2*, the transverse magnetization begins to decay [37]. T1, T2 and T2* are time parameters that denote how fast the protons fall back to their equilibrium energy state, i.e. the time of relaxation.

As the relaxation processes occur independently but simultaneously, the NMV is then the sum of the longitudinal and transverse magnetizations. The change of the magnetic moments of the NMV following the application of an RF pulse results in a free induction decay (FID). This results in a RF signal that is captured by an RF receiver coil and processed to obtain localized information about the protons in the patient's tissues [40]. This process of giving energy to the spins and then receive the energy released as the spins relax is the basis of MR imaging [40].

2.3.5 K-space

The RF signal captured is received by a computer and processed by an analog/digital converter. The digital signal corresponding to the body part imaged is stored in a data matrix form, the k-space (Figure 2.13). Each point of the k-space contains specific frequency and phase (*x* and *y* coordinates of the matrix) and signal intensity information regarding every pixel in the image [39]. The k-space matrix stores MRI signals during data acquisition and, after applying an inverse Fourier transform to it, an image of the imaged body region is obtained.

The image produced is composed by pixels, which are picture elements. Each picture element in the resultant image is the weighted sum of all the individual points in the k-space and corresponds to a volume element (voxel) of the body part imaged [39].

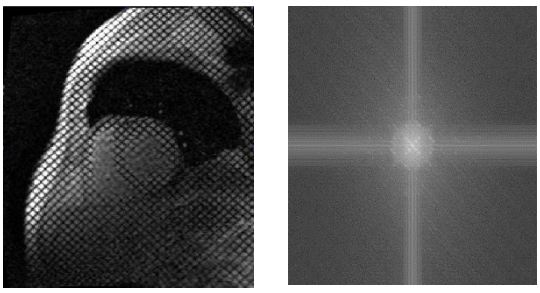

Figure 2.13: Example of a cardiac MR image (left) and the corresponding k-space (right).

2.3.6 Pulses sequences

Pulses sequences are a pattern of RF pulses and magnetic gradients that are used to produce an image. The echo time (TE) and repetition time (TR) are important parameters of the pulse sequences and are responsible for the image contrast.

The TE refers to the time between the application of RF pulse and the peak of the signal (echo) induced in the coil. It sets how much the transverse magnetization is allowed to decay between each pulse and it is measured in ms. When TE is short, there is a short time for T2-decay to take place and hence the tissues are not differentiated. The T2-weighted image must have a long enough TE so that the relative differences in signal decay between different tissues becomes clearer. The amount of T2-weighting is then controlled by TE [41].

The TR time is the time between the application of consecutive RF pulses. It determines how far longitudinal magnetization recovers between pulses and it is measured in ms [41]. A T1-weighted image must have a short TR so that the spins in different tissues won't have time to return to full B_0 alignment before the echo, which allows the signals from the tissues to be differentiated. Therefore, TR controls the amount of T1-weighting.

Gradients are relatively small varying magnetic fields that are applied in addition to the large constant magnetic field B_0 causing spins at different locations to precess with slightly different frequencies or phases [40]. There are three types of gradients according to the three directions of spatial encoding: slice-select, frequency-encoding and phase-encoding gradients.

The slice-select gradient is imposed along an axis perpendicular to the slice plane and the frequency of the RF pulses is set to match the narrow range of frequencies contained in the desired slice. This ensures that only spins within the chosen slice are excited.

After slice selection, the phase-encoding introduces phase-shifts in the spins along one axis in the plane of the slice, and the frequency-encoding gradient then changes the precession frequencies of the spins along an orthogonal axis in the slice plane. Thus, the frequencies and phases of the spins in the slice will vary as a function of position.

Spin echo (SE) sequences (Figure 2.14) include a 90º pulse followed by a 180º refocusing pulse [37]. After the spins have been excited by a 90° pulse, the spins dephase in the transverse plane. After a time TE/2, the spins are exposed to a 180° pulse and the refocusing is initialized, which creates an echo at time TE. The position of the spins has not changed and they will continue precessing and with the same frequency.

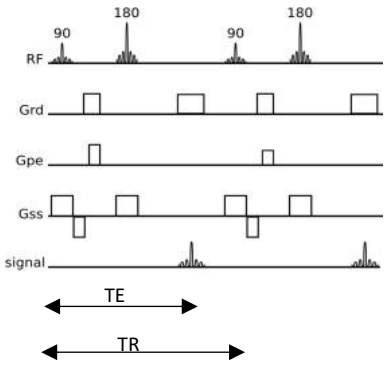

Figure 2.14: Timing diagram of a SE pulse sequence. Radio frequency pulses (RF), Frequency-encoding gradient (Grd), Phase-encoding gradient (Gpe), Slice-select gradient (Gss), Echo time (TE), Repetition Time (TR) Adapted from [42].

In SE sequences, only one line of k-space is acquired for each TR, which increases the acquisition time for each slice. Fast spin echo sequences can be used instead of SE in order to achieve faster acquisition times. It uses a series of 180º refocusing pulses after a single 90º pulse to generate a series of echoes [37]. As it changes the phase-encoding gradient for each of the echoes, multiple lines of k-space can be acquired during a TR, which significantly reduces imaging time.

Gradient echo (GE) (Figure 2.15) is generated by a single RF pulse lower than 90º in conjunction with a frequency-encoding gradient [37]. The consequence of having an RF pulse lower than 90º is the decrease of the amount of magnetization tipped into the transverse plane, allowing the longitudinal magnetization to recover faster. As there is no 180° RF pulse, a gradient is required to create an echo. The gradient is then responsible for causing a dephasing of the precessing spins in the transverse plane and when this gradient is reversed, the dephased spins re-align and form a GE.

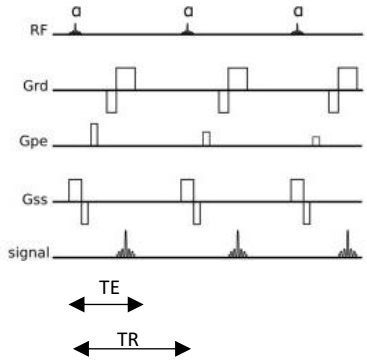

Figure 2.15: Timing diagram of a GE pulse sequence. Radio frequency pulses (RF), Frequency-encoding gradient (Grd), Phase-encoding gradient (Gpe), Slice-select gradient (Gss), Echo time (TE), Repetition Time (TR). Adapted from [42].

SE sequences are associated to longer acquisition times, but are less susceptible to artifacts due to the presence of metals than GE. The longer acquisition times are caused by the presence of the 180º RF pulse, which is not present in GE sequences. The artifacts due to metals happen because the 180º RF pulse in a SE sequence compensates for the static field inhomogeneities due to metal or other magnetic fields variations [43]. As the pulse rephases only static field distortions in the interval between RF excitation and echo formation, it means that the transversal decay in SE is due to T2 only. In GE there is no 180º RF pulse, so that these sequences are more prone to metal artefacts because the transverse magnetization decays accordingly to T2* and not only T2 [37].

There are a variety of different pulse sequences that are used in cardiac imaging that can be broadly divided into either black-blood techniques or bright-blood techniques. In black-blood images, the blood inside the heart appears as dark as the MR signal from the blood is suppressed. In bright-blood techniques, the MR signal from the blood is retained and so the blood is bright. SE cardiac sequences are typically black-blood techniques, while GE sequences are typically bright-blood techniques.

Black-blood effect (Figure 2.16) occurs only in SE due to the existence of the 180° pulse. The tissues in a slice receive both 90° and 180º pulses and an echo is produced. But if the blood that was in the slice when the 90° pulse was applied, has left the slice by the time the 180° pulse

is applied at TE/2, it means that at the time of the 180° pulse, the blood in the slice will not have received the 90° pulse. So, there will be no magnetization from the blood in the transverse plane to produce an echo. When blood flows out of the slice, the signal from flowing blood is suppressed while maintaining high signal in the surrounding stationary tissues. This is the reason the intracavitary blood appears as dark while the myocardium and other surrounding tissues are bright [44].

Black-blood imaging provides detailed morphological images of the heart, pericardium, and great vessels [44]. The myocardium has a grey appearance, similar to that of skeletal muscle, and is clearly distinguishable from the adjacent bright epicardial fat and dark intracavitary blood.

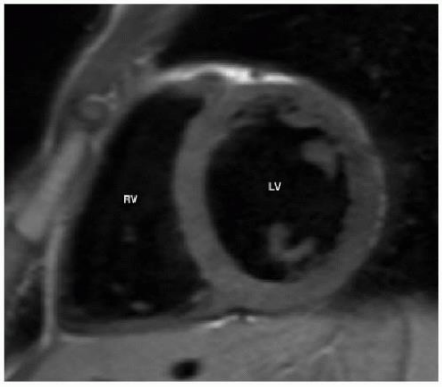

Figure 2.16: Black-blood T1-weighted short axis image through the mid aspect of the right and left ventricles (RV and LV). The grey appearance of the myocardium is clearly distinguishable from the dark intracavitary blood [44].

In bright-blood techniques (Figure 2.17), the magnetization of the tissues in the slice becomes partially saturated. Then, the longitudinal magnetization does not recover between each repetition of the pulse sequence. Nevertheless, blood outside the imaging slice has no prior RF pulses applied to it. If this blood flows into the slice, then its full longitudinal magnetization will produce a brighter signal when a portion of it is flipped into the transverse plane by the 90º pulse [44].

Bright-blood imaging is used in the assessment of ventricular function, blood velocity and flow measurements, valvular disease and myocardial perfusion [44]. Considering its high spatial and contrast resolution, image quality of cine images is often superior to black-blood images.

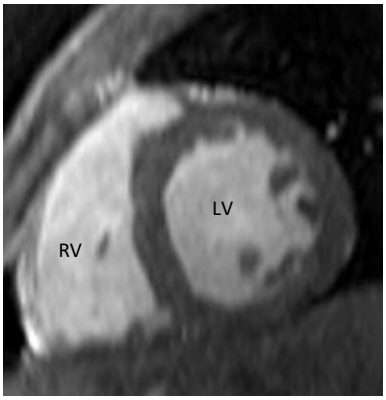

Figure 2.17: Bright-blood T1-weighted short axis image through the mid aspect of the right and left ventricles (RV and LV). The dark appearance of the myocardium is clearly distinguishable from the bright intracavitary blood [44].

Steady State Free Precession (SSFP) is a type of GE sequence, which uses steady states for both components of magnetization (transverse and longitudinal) and also obeys the condition of having a TR shorter than the T1 and T2 relaxation times of the tissue. If the RF pulses are close enough in time, the MR signal will never completely decay, implying that the spins in the transverse plane never completely dephase. So, SSFP is a modification of GE imaging that produces bright blood images with excellent contrast and high temporal resolution between myocardium and intracavitary blood (Figure 2.18) [37]. This technique improved the cardiac perfusion and function assessment.

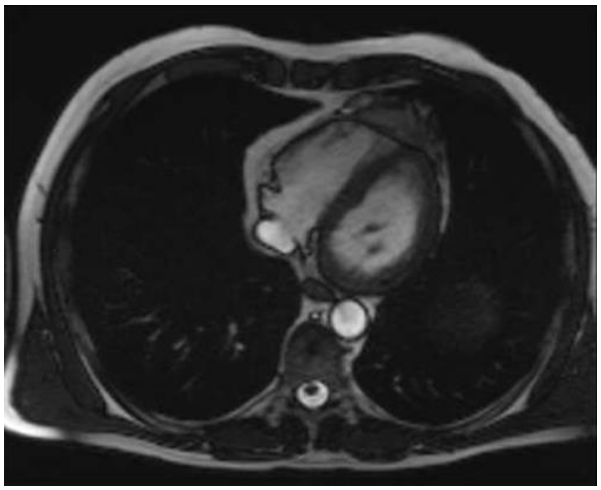

Figure 2.18: Steady State Free Precession (SSFP) showing the excellent contrast between the myocardium and the intracavitary blood. Adapted from [45].

2.4 Cardiac MRI

2.4.1 Data acquisition

MRI is widely used in the medical community. It uses a combination of a large strength magnet of 1.5 T or 3 T, RF and gradient coils (Figure 2.19), and a computer to produce detailed images. With a scan period of 30-45 min, cardiac and pericardial morphology, systolic and diastolic functional indices, valvular function and myocardial perfusion can be assessed.

Figure 2.19: 1.5 T MRI scanner used in cardiac MRI (left) and a RF coil (right) to be placed on the patient's chest during MRI scan. Adapted from [46].

The most common challenge of cardiac MRI image acquisition is overcoming motion artifacts. [47]

Motion artifacts due to the respiratory process can be eliminated by breath holding technique. In this technique, cardiac scans are normally performed under exhalation period, as during inhalation there is a diaphragm movement and consequent anatomical positioning changes. It is therefore very important to give proper instructions to the individuals for them to know how should they proceed during the exam. The patient should firstly be instructed to breathe in, although not too deeply, secondly to breathe out, to stop breathing, and finally to breath normally after the scan [47].

Motion artifacts arising from the cardiac cycle can only be eliminated by ECG gating, which can be done using either prospective or retrospective triggering.

In prospective triggering (Figure 2.20), the data is acquired only during a specified phase of the cardiac cycle, typically between R waves. The data is acquired at the same cardiac cycle time, across multiple cardiac cycles.

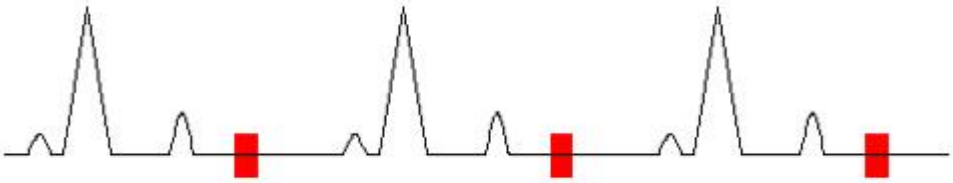

Figure 2.20: Prospective triggering. The ECG is traced with the red rectangle boxes representing the acquisition periods. The data is acquired at the same cardiac cycle time, across multiple cycles. Adapted from [47].

In retrospective triggering (Figure 2.21), the data acquisition in the cardiac cycle begins with the R wave of the ECG and ends with the next R wave. Each R-R period is typically divided into 10 to 20 frames, depending on the heart rate, and each frame is composed of information gathered over several heartbeats. This type of ECG gating is used to obtain images from all phases of the cardiac cycle, as in cine images (sequence of frames displayed like a movie), which are helpful on analyzing cardiac function and heart wall motion.

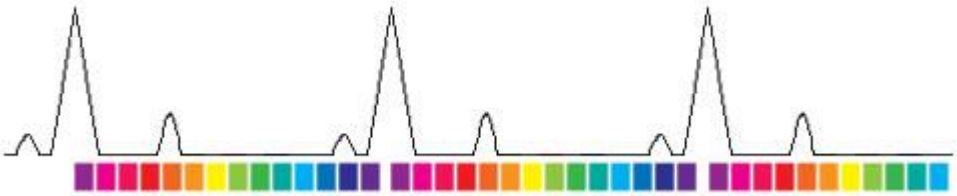

Figure 2.21: Retrospective triggering. The ECG tracing with the colored rectangle boxes representing different frames. Data is acquired during the same time frame across multiple cycle to produce an image. The series of images originates cine images (sequence of frames displayed like a movie). Adapted from [47].

2.4.2 Cardiac axes and imaging planes

In order to provide the correct diagnosis, it is necessary to possess proper clinical information before the study onset, enabling the MRI examination to be fine-tuned using appropriate sequences and imaging planes.

The three orthogonal planes generally used for imaging are the frontal, sagittal and transversal. However, as the orientation of the heart differs from the human body and general axes, it is usually studied along three intrinsic cardiac axes, i.e., vertical long axis (two-chamber view), horizontal long axis (four-chamber view) and short axis (SA). The vertical long axis of the heart is not parallel to the long axis of the body, but is rotated about 45º to both sagittal and coronal axes instead [48]. Therefore, cardiac MRI is able to image the heart through these cardiac axes.

The vertical long axis (two-chamber view) is represented in Figure 2.22 and is also used for evaluating the anterior and inferior walls and apex of the left ventricle. From a transversal image through the LV and LA, this view is achieved by a perpendicular plane that bisects the mitral valve and intersects the LV apex.

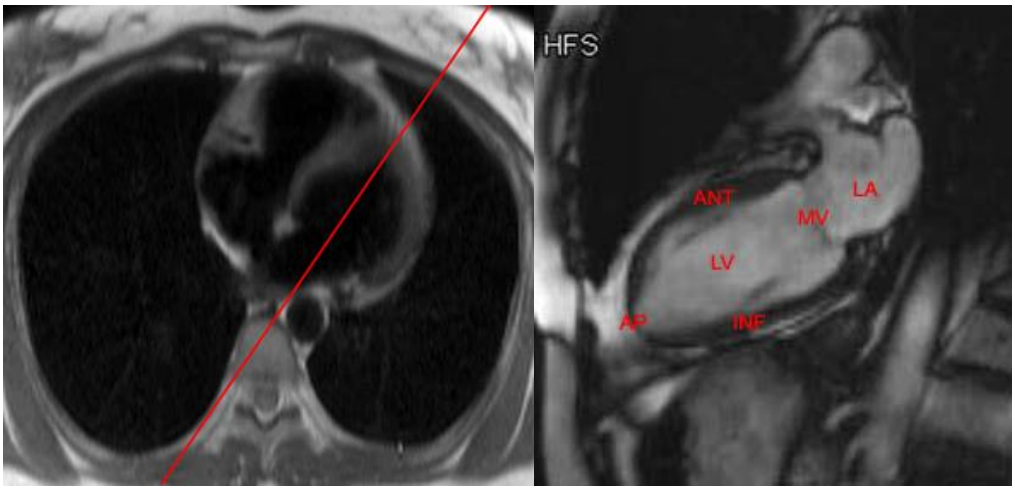

Figure 2.22: The red line in the figure on the left represents the plane through which the vertical long axis image on the right is obtained. Anterior wall (ANT), Apex (AP), Inferior wall (INF), Left Atrium (LA), Left Ventricle (LV), Mitral Valve (MV). Adapted from [46].

The horizontal long axis (four-chamber view) is best for evaluating the septal and lateral walls, the apex of the left ventricle, and the chamber size. This view is achieved by a perpendicular plane to the vertical long axis image that intersects the lower third of the mitral valve and the LV apex, as represented in Figure 2.23. The mitral and tricuspid valves are also well visualized in this plane.

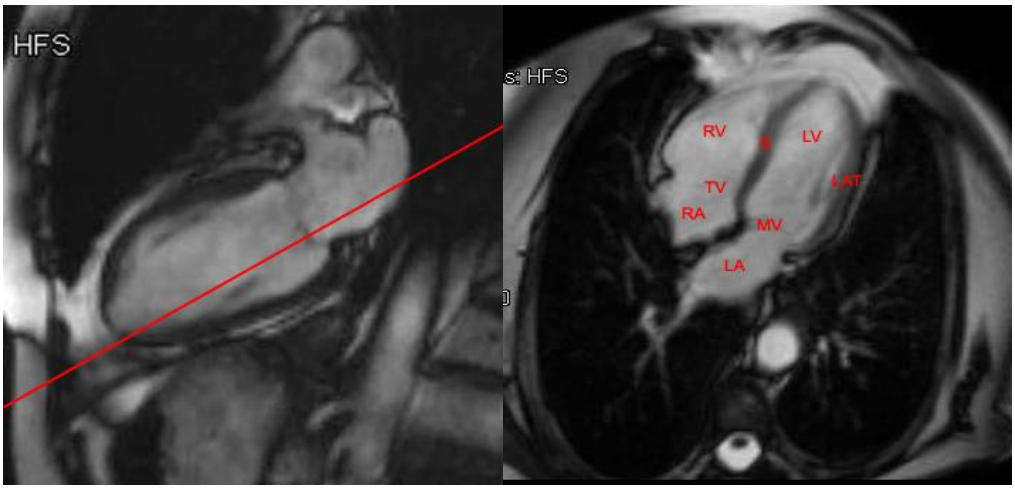

Figure 2.23: The red line in the figure on the left represents the plane through which the horizontal long axis image on the right is obtained. Lateral wall (LAT), Right Atrium (RA), Right Ventricle (RV), Tricuspid Valve (TV), Septum (S), Left Atrium (LA), Left Ventricle (LV), Mitral Valve (MV). Adapted from [46].

The SA view (Figure 2.24) shows cross-sections of the left and right ventricles that are useful for volumetric and strain measurements. The SA view is chosen such that the slices are perpendicular to the long axis of the LV.

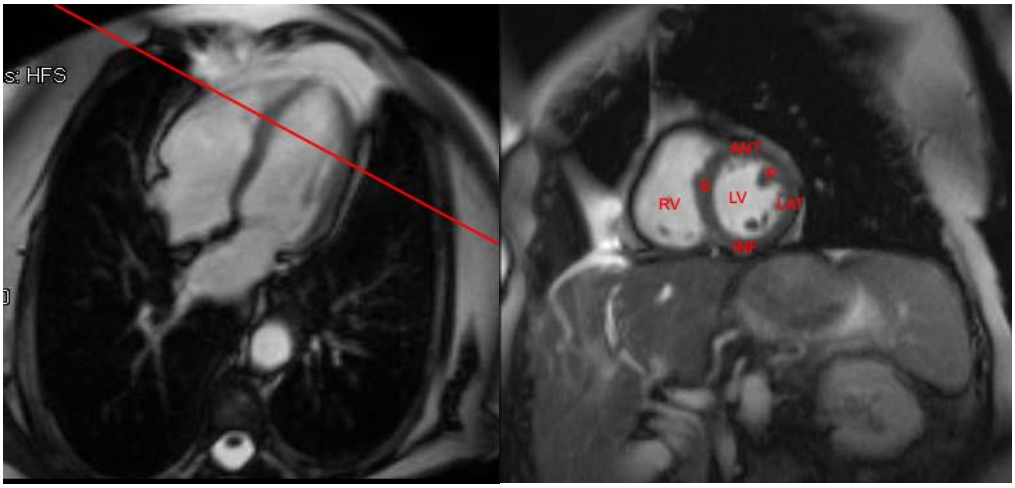

Figure 2.24: The red line in the figure on the left represents the plane through which the short axis image on the right is obtained. Anterior wall (ANT), Inferior wall (INF), Lateral wall (LAT), Left Ventricle (LV), Papillary muscle (P), Right Ventricle (RV), Septum (S). Adapted from [46].

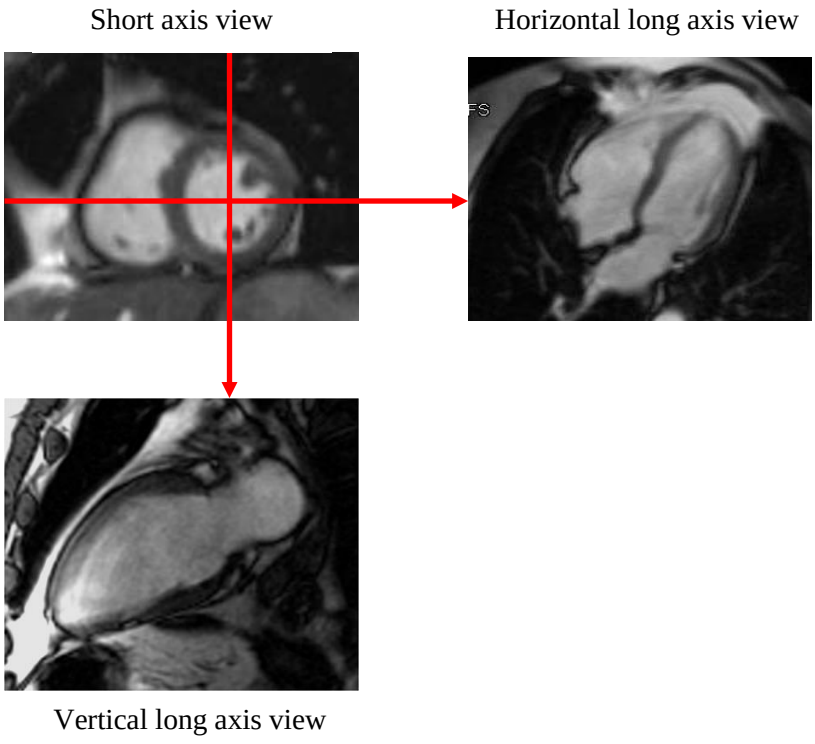

Figure 2.25: Relation between the short axis view and the other axes view. Adapted from [46].

There are many advantages in cardiac MRI when compared to other noninvasive imaging modalities such as ultrasound and CT. MRI does not employ ionizing radiation, thus permitting its use in children and pregnant women. It can produce high resolution and three dimensional

(3D) images of the cardiac chambers and blood vessels. Unlike echocardiography, MRI can produce images of cardiovascular structures without interference from adjacent bone or air as in echocardiography. MRI does not have the limitation of geometric assumptions imaging in assessing ventricular volumes as 2D echocardiography. Most new aneurysm clips, stents and vascular filters are MR compatible.

However, cardiac MRI has several disadvantages. MRI requires more patient cooperation in order to have a better image quality, for example during breath holds. Also, claustrophobic patients may be incapable to undergo the exam. Examination times are significantly longer as compared with CT and X-rays. This, in addition to the fact that the patient is physically isolated from direct care when inside the scanner, makes MRI unsuitable for unstable patients. Installation and operation of MRI equipment is costly and as such is an important consideration both for hospitals and patients. Due to the forceful attraction of ferromagnetic objects to the magnets in MRI scanners, most intracranial or intraocular metal, cardiac pacemakers, and cochlear implants are absolute incompatible with MRI.

2.5 Cardiac motion strains

MR signal has long been known to be sensitive to motion. One of the main reasons for motion sensitivity is that when the local magnetization of a material is altered, the material maintains the altered magnetization (within the limits of the relaxation times) when it moves.

Therefore, cardiovascular magnetic resonance (CMR) imaging excels in terms of tissue contrast, spatial resolution, and signal-to-noise ratio (SNR), allowing more detailed analysis to take place while remaining noninvasive and without using ionizing radiation. The advent of cardiac MRI tagging, which is explained later in section 2.6, has been established as an essential technique for measuring regional myocardial function since it allows the identification of local myocardial motion measures, e.g. strain.

The ventricular contraction is initiated by electrical stimulation of the thick-walled myocardium, causing an increase in tension and shortening of myocytes, which is translated into a myocardial strain. It is defined as the change of shape at any point in the wall between the original reference state and the subsequent deformed state [49]. The infinitesimal strain (2.1) is given by:

$$\varepsilon_{ij} = \frac{1}{2}\left(u_{i,j} + u_{j,i}\right) = \frac{1}{2}\left(\frac{\partial u_i}{\partial j} + \frac{\partial u_j}{\partial i}\right) \tag{2.2}$$

where *i,j= x, y, z* are the three spatial coordinates, *ui* is the myocardial wall displacement in direction *i* and $u_{i,j}$ is the myocardial wall deformation gradient (see Figure 2.26). In case the deformation is on the *x* direction (*i,j= x)*, then the equation would be:

$$\varepsilon_{xx} = \frac{1}{2}\left(\frac{\partial u_x}{\partial x} + \frac{\partial u_x}{\partial x}\right) = \frac{\partial u_x}{\partial x} = \frac{\text{length in deformed state(x) – original length(x)}}{\text{original length(x)}} \tag{2.3}$$

in which the deformation in the *x* direction is given by the variation of the length divided by the original length in that direction.

εij is represented by a symmetric 3x3 tensor of myocardium's length change normalized to its original length and it is dimensionless.

$$\varepsilon_{ij} = \begin{bmatrix} \varepsilon_{xx} & \varepsilon_{xy} & \varepsilon_{xz} \\ \varepsilon_{yx} & \varepsilon_{yy} & \varepsilon_{yz} \\ \varepsilon_{zx} & \varepsilon_{zy} & \varepsilon_{zz} \end{bmatrix} \tag{2.4}$$

$$\varepsilon_{ij} = \begin{bmatrix} \frac{\partial u_x}{\partial x} & \frac{1}{2}\left(\frac{\partial u_x}{\partial y} + \frac{\partial u_y}{\partial x}\right) & \frac{1}{2}\left(\frac{\partial u_x}{\partial z} + \frac{\partial u_z}{\partial x}\right) \\ \frac{1}{2}\left(\frac{\partial u_y}{\partial x} + \frac{\partial u_x}{\partial y}\right) & \frac{\partial u_y}{\partial y} & \frac{1}{2}\left(\frac{\partial u_y}{\partial z} + \frac{\partial u_z}{\partial y}\right) \\ \frac{1}{2}\left(\frac{\partial u_z}{\partial x} + \frac{\partial u_x}{\partial z}\right) & \frac{1}{2}\left(\frac{\partial u_z}{\partial y} + \frac{\partial u_y}{\partial z}\right) & \frac{\partial u_z}{\partial z} \end{bmatrix} \tag{2.5}$$

Lagrangian (2.5) and Eulerian (2.6) strains are examples of strain tensors that can be used to calculate circumferential and radial strains. I is the identity tensor and F is the deformation gradient tensor. Both tensors are very similar but in Lagrangian strain, the deformation reference state for strain calculation is before deformation takes place, while in Eularian strain it is after the deformation. When the deformation gradients are small, both strains approximate the infinitesimal strain (2.4), which means that myocardial wall strain can be equally calculated from Infinitesimal, Langrangian or Eularian strain tensors, as explained in section 2.6.

$$\varepsilon_{ij} = \frac{1}{2}(F^T.F - I) \tag{2.5}$$

$$\varepsilon_{ij} = \frac{1}{2}(I - F^T.F^{-1}) \tag{2.6}$$

The three components of the infinitesimal strain tensor diagonal are the normal components, representing tensile and compressive loading along the three coordinate axes directions (Figure 2.26). Positive normal strains are associated with tension or stretch, while negative normal strains describe shortening or compression in relation to the original length [50]. The deformation of the myocardium also depends on its position and orientation, and varies in time through the cardiac cycle.

As the components of the strain tensors depend on the chosen frame of reference, it is conventional to choose an orthogonal system, such as local circumferential, longitudinal and radial axes for analyzing myocardial deformations (Figure 2.27). The off-diagonal elements are the shear-strain components, associated with the off-axis distortions of the wall such as torsion due to the rotation of the apex relative to the base. Given this, positive radial strain represents the myocardial thickening in a short axis plane, negative circumferential strain represents myocardial shortening in a short axis plane and negative longitudinal strain represents the myocardial shortening in the long axis plane [51]. During myocardial contraction, as the wall shortens it also thickens and thus assessment of all parameters, radial thickening (positive strain), circumferential shortening (negative strain) and longitudinal shortening (negative strain), is useful for the evaluation of LV contractile function.

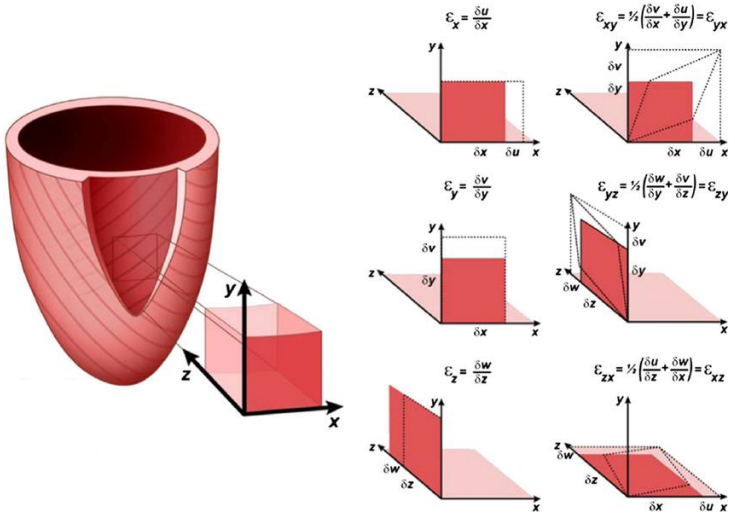

Figure 2.26: Myofiber architecture and 3D deformation of the left ventricle. The left panel shows a schematic representation of the myocardial fiber orientation in the subendocardial and subepicardial regions of the left ventricle. The panels in the center and to the right show the three components of normal (center) and shear strain (right) in a myocardium section. Adapted from [52].

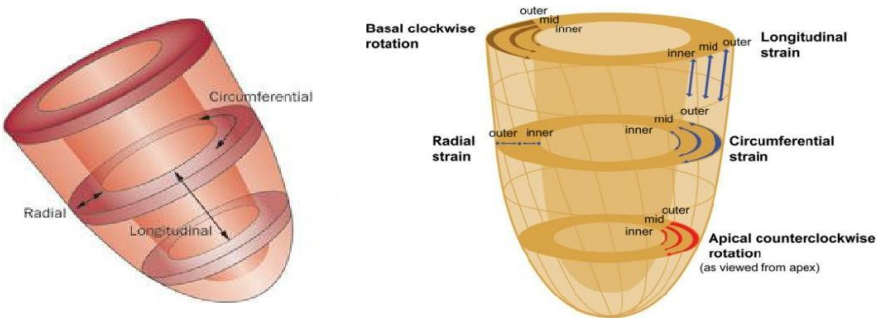

Figure 2.27: Left Ventricular Strains: Circumferential, Radial and Longitudinal. Adapted from [53] [54].

The highly complex myofiber anatomy with profound differences in myocardial fiber orientation is not random but in fact represents a powerful mechanism to enhance the efficiency of single-fiber shortening. Toward endocardium and epicardium, fiber orientation becomes progressively oblique in opposite directions, which takes these fibers into an almost perpendicular orientation to each other [52]. On the other hand, longitudinally orientated fibers, except in papillary muscles, are sparse in the LV wall. Because of this fiber orientation, myocardial and ventricular deformation consists in a combination of circumferential and longitudinal shortening, radial thickening, and shear motions (ventricular torsion) as described before. Circumferential LV shortening with centripetal wall motion is primarily caused by midwall fiber contraction, whereas longitudinal shortening is largely the result of contraction of the oblique epicardial and endocardial fibers. Radial thickening is caused by a transmural interaction between the oblique epicardial and endocardial fibers [52].

The major goal of regional cardiac mechanical analysis is to quantify and characterize regions of altered mechanical function and correlate this with alterations in perfusion, structure, and metabolism of the heart. As a host of physiological and pathological processes are directly or indirectly regulated by regional myocardial strain, including acute ischemia, myocardial infarction, hypertrophic and dilated cardiomyopathies, and arrhythmias, these data are valuable for identifying the risk of disease progression [49].

2.6 Measuring LV strains using MRI

As previously mentioned, anatomical images show the inner and outer borders of the heart, which upon segmentation provide valuable measures about the heart global function, e.g. ejection fraction and myocardial thickness. Regional myocardial functions such as strain and torsion allow the early identification of dysfunction and the evaluation of heart condition. Their measurement is therefore extremely important for clinical risk assessment, patient treatment and therapeutic efficiency.

The measurement of regional myocardial functions was originally done by surgical implantation of physical markers as radiopaque materials [55] or ultrasound crystals [56] and imaging the implants motion. Sonomicrometry [59] is a technique which consists of implementing the crystals inside the myocardium and measure the distance between them during the whole systole, by detecting a sound signal that passes through the crystals until it reaches a receiver. The invasive implantation of these markers into the heart wall enabled tracking tissue material points within the myocardium and thus measuring local tissue deformation between the tracked markers. Due the fact that it is an invasive method, the implantation process has some limitations, as the possibility to modify the tissue motion due to the application of the implants. Therefore, this technique cannot be applied repeatedly.

The invention of non-invasive method to measure myocardial motion came in the late eighties, where the technique CMR tagging allowed for the first time to visualize transmural myocardial displacement without the need to implant physical markers. By quantifying intramyocardial wall motion non-invasively, CMR tagging proved to be a valuable and safe tool for cardiovascular imaging. The CMR tagging method has been established as an essential technique for quantitative measurement of regional intramyocardial strain. In 1988, Zerhouni et al. [57] introduced the idea of myocardial tissue tagging, a noninvasive technique based on applying slice-selective RF pulses perpendicularly to the imaging plane, which perturbs the longitudinal magnetization and creates visible markers that can be imaged and tracked. The technique allowed for the first time to visualize transmural myocardial displacement without having to implant physical markers. CMR tagging technique was validated in a study [58], in which the correlation between systolic wall thickening by CMR tagging and by sonomicrometry was examined. The results showed a strong correlation between the two techniques [58].

After the creation of tagging by magnetization saturation, a more efficient CMR tagging technique was invented, the Spatial Modulation of Magnetization (SPAMM) [60]. Both methods rely on the creation of a visible pattern of magnetization saturation on the magnitude reconstructed images, usually parallel lines or a grid pattern. This allows the visualization of myocardial contractility without any post-processing. Nevertheless, exhaustive and extensive post-processing is needed to identify and track myocardial tags and to quantify myocardial motion [61].

In order to track the tags during the whole cardiac cycle, the MR images are represented by a sequence of multiple frames as a short movie, the CINE images [62]. Each image corresponds to a cardiac cycle frame but is composed of information gathered over several heartbeats, allowing for a movie to be a sequence of individual frames during a single heartbeat. These images can be very helpful in studying how myocardium contracts and thickens throughout the cardiac cycle and therefore to analyze cardiac function.

In 1999, an invention of Harmonic Phase (HARP) allowed the faster and more automatic analysis of myocardial motion than in the previous tagging techniques [61]. HARP technique is centered in a k-space perspective of spectral peaks corresponding to the tagging frequencies, where HARP image is obtained by the inverse Fourier Transform (FT) of the peaks. The motion of a tissue point on the tag lines is tracked by its constant harmonic phase during the cardiac motion and the mechanical strain of the tissue can also be estimated through the gradient of the harmonic phase from frame to frame [63]. The efficiency of HARP is, however, limited by the wrapping effect, i.e. there could be more than one point on the tag lines that have the same harmonic phase because of the periodicity of the tagging. To prevent the wrapping effect, the deformation between two successive MRI images should be small and, therefore, there must be enough number of MRI images to cover a cardiac cycle.

While SPAMM is very straightforward in the visualization of myocardial deformation during cardiac cycle, the tracking and detection of the tag lines require a long post-processing effort. On the other hand, HARP has the advantage of requiring a simpler post-processing to yield motion information but it is more sophisticated and less straightforward to implement than the SPAMM technique. The SPAMM and HARP techniques are described next.

2.6.1 SPAMM

The tagging idea presented by Zerhouni et al. [60] led to the invention of a more efficient tagging technique by Axel and Dougherty in the following year, which is still in use until today, the SPAtial Modulation of Magnetization (SPAMM). The technique is based on modulating the myocardial magnetization periodically in space by applying two similar nonselective RF pulses separated by a wrapping (modulating) gradient before imaging. The resulting tagged regions appear as periodic stripes and their displacement reflect the cardiac motion occurred between tagging and imaging time [57].

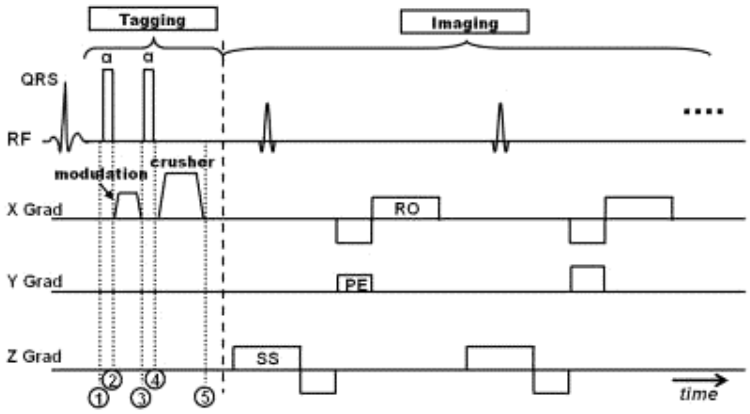

Figure 2.28: SPAMM pulse sequence diagram. The tagging part consists of only two non-selective RF pulses (usually, 90° each), separated by the modulation gradient and followed by a large crusher gradient. The imaging part shows k-space acquisition (RO = readout, PE = phase encoding, SS = slice selection). This sequence creates parallel tag lines orthogonal to the x-axis; At time point 1, the magnetization is at equilibrium state in the longitudinal direction. The first RF pulse is applied, which tips the magnetization into the transverse direction. At time point 2, the tagging gradient disperses the spins in the tagging direction (x-direction in this case). By the end of the gradient pulse (time point 3), the spins are modulated by incremental phase shifts along the x-axis. The second RF pulse tips the resulting modulated magnetization into an opposite direction to the first RF pulse (time point 4). A crusher gradient immediately follows to remove transverse magnetization, leaving only the longitudinal magnetization. Adapted from [61].

There are two stages in this technique, the tagging and the imaging (Figure 2.28). Normally, tagging is implemented at end-diastole after the detection of the R-wave in ECG, and imaging takes place at end-systole, to assess the heart muscle condition at maximum contraction.

The tagging stage starts from a condition of uniform longitudinal magnetization, where the first RF pulse turns the magnetization into transverse magnetization with all spins in phase. A gradient pulse immediately follows along the desired tagging direction, which produces a spatial modulation of the phase depending on the spatial location of spins. This gradient has the effect of modulating the magnetization along the gradient direction through incremental phase shifting of the spins in this direction. A second RF pulse has the same flip angle as the first one and combines the modulated transverse magnetization with the longitudinal magnetization, allowing the modulated magnetization to be restored into the longitudinal direction. A large 'crusher' gradient follows the second RF pulse to eliminate any remaining transverse magnetization before image acquisition.

Alternatively, if grid tagging is required, a second tagging stage immediately follows the first stage with a modulating gradient oriented in an orthogonal direction to the first one. The grid can be produced by another RF pulse with a second modulating gradient in an appropriate direction and then with a final RF pulse.

The tagging stage is then a spatially modulation of the longitudinal magnetization and this process is followed by the imaging stage.

The imaging acquisition stage consists of a series of slice-selective RF pulses followed by phase encoding and readout gradients for k-space filling, as explained in section 2.3. This results in images showing dark periodic stripes in the tagged areas due to the modulation, where the stripes are bands of oscillating signal intensity across the image that translate the spatial variations of magnetization. These strips correspond to the intersection of the modulation bands with the imaged section. Also, the orientation of the stripes is determined by the direction of the wrapping gradient and the separation between them is inversely proportional to the strength and duration of the wrapping gradient [60]. Because magnetization is an intrinsic property of the underlying tissue, the stripes move with the tissue. In the moving tissue, the motion between the tissue tagging time with SPAMM and tissue imaging time corresponds to the displacement of the stripes.

Figure 2.29: Myocardial SPAMM grid-tagged image at end-diastole (left) and end-systole (right). The tag lines applied on the myocardium by using SPAMM deform along during systole.

If there is a specific motion restrict to a part of the FOV (field of view), a uniform tagging grid that covers the whole image plane may not always be desirable. Localized SPAMM offers an alternative to conventional SPAMM and it is suitable for applications where the motion to be studied is limited to specific areas of the image. In this case, the tagging grid can be limited to the

area of motion, keeping the rest of the image intact to preserve the anatomical information. Additionally, some studies have been conducted to create variable tagging density. In 1998, McVeigh and Bolster [64] presented a method for producing variable separation tagging to improve the tags displacement detection during systole. In regions of the image where the tags increase their separation due to the deformation, the tag planes are placed further closed at end-diastole and in regions where the tags decrease their separation, the tags are placed further apart. As the tags are placed further closer or apart during end-diastole, which corresponds to the non-deformed state of the tags, the deformations between the tags are even more highlighted at end-systole, which is the deformed state. The tag lines separation was customized to match the expected motion of specific regions (e.g. the myocardium wall). The only limitation of the variable separation tagging is its duration but with this method, parallel plane tagging can be used to obtain higher resolution estimates of radial thickening and circumferential shortening.

From figure 2.29, it is possible to see that tagged areas show a darker signal intensity, which is represented by the stripes, in comparison to non-tagged areas. Longitudinal relaxation has the effect of restoring the equilibrium condition of the tagged magnetization with exponential rate depending on T1. Therefore, the longer the time duration between tagging and imaging, the lower the contrast between the tagged and non-tagged tissues will be. When the quality of SPAMM tagged images was compared at 3.0 Tesla (T) and 1.5T, the results showed that imaging at 3.0T benefits from the longer myocardial T1, which results in better tagging contrast persistence through the cardiac cycle as the tags do not fade away in such a short time. [65].

Besides the limitations of the low spatial resolution of the tags and their fading during diastole, SPAMM is already used in routine clinical CMR exams and in some studies, such as myocardium wall motion. It is also useful for assessing ventricular function, as the areas of myocardium that are not contracting appropriately will demonstrate decreased deformation of the grid during the cardiac cycle.

2.6.2 HARP (HARmonic Phase)

Harmonic phase magnetic resonance imaging (HARP) has been developed to measure and quantify the LV strain using MR tagging [66]. HARP combines the SPAMM tagging technique with image processing algorithms to quantify myocardial motion including radial and circumferential strains. SPAMM modulates the underlying image with tags, which appear in the respective 2D FT as an array of spectral peaks at harmonics of the tagging frequency. Each of these spectral peaks carries information about a particular component of tissue motion and this information can be extracted by filtering the spectral peaks with a bandpass filter.

The inverse FT of a peak is a complex image whose calculated angle is called harmonic phase [67] [68]. The goal in HARP is to extract the peak at the first harmonic frequency, which contains the tagging information (Figure 2.30-b). After applying the FT, magnitude and phase images are obtained and both harmonic images are necessary for HARP analysis. The harmonic phase image (Figure 2.30-d) shows intensity gradients interrupted by sharp transitions resulting from phase wrappings every 2π, while the magnitude image (Figure 2.30-c) is blurry due to the filtering process. When multiplied together, the phase and magnitude images result in a new image, the HARP image (Figure 2.30-e), which is very similar to the original tagged image but in this case, the pattern represents the wrapped tissue phase instead of the tagging.

In the k-space of a harmonic image, the major spectral energy is concentrated in the spectral peaks (Figure 2.30-b). Therefore, the size and position of the bandpass filter should be properly positioned to capture the spectral energy, which also changes during the cardiac cycle according to the heart strain. Myocardial tissue stretching will lead to a decrease in the magnitude of the central peak and myocardial tissue contraction will cause an increase in the central peak magnitude [69]. The bandpass filter should be a circular shaped mask centered in the maximum frequency of the spectral tagging peak and it should have a radius equal to approximately 50% of the maximum tagging frequency of the peak [66].

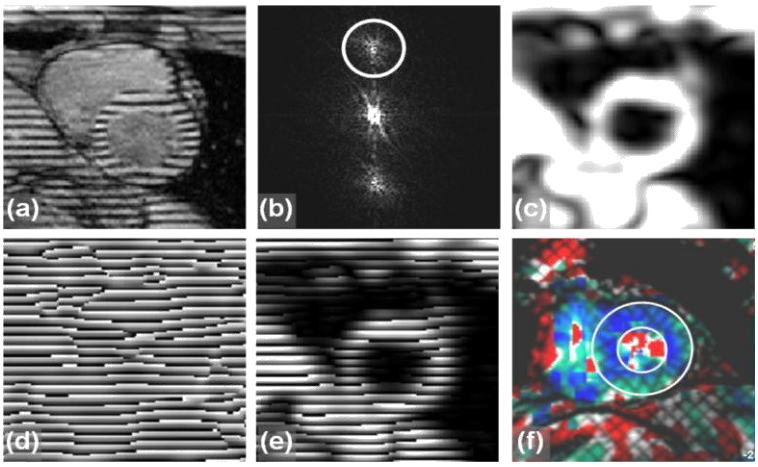

Figure 2.30: HARP tagging of the LV: (a) SPAMM tagged image of LV. (b) K-space of SPAMM image with the spatial band-pass filter to extract only the first harmonic peak. (c) Harmonic magnitude image obtained from the FT in (b). (d) Harmonic phase image obtained from the FT in (b). (e) HARP image resulting from the multiplication of harmonic magnitude and phase images. Myocardium displacement tracking can be conducted by simply tracking the tissue phase from frame to frame. (f) An example of a grid-tagged image analyzed with HARP, which shows myocardial circumferential strain [61].

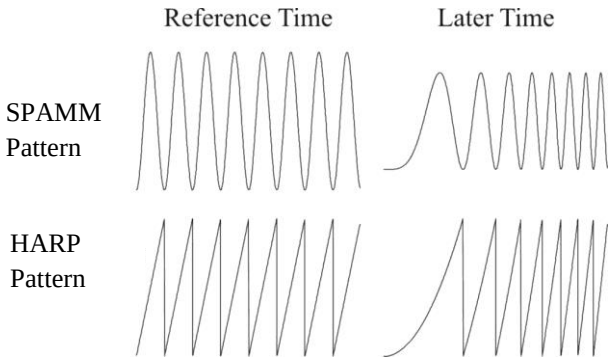

Figure 2.31: Sinusoidal patterns of tags spatial frequencies in SPAMM (top) and HARP (bottom) images in end-diastole (reference time) and at end systole (later time). As the tags fade during cardiac cycle, the amplitude of the sinusoids decreases. The frequency is decreased in end diastole (myocardial stretch) and increases in end systole (myocardial contraction). Adapted from [69].

Figure 2.31 shows that both HARP and SPAMM images are very similar and experience the same changes in terms of tags frequencies during cardiac cycle. The image tags fade from end-diastole (reference time) to end-systole, which is translated into a decrease in amplitude and frequency changes in the sinusoidal pattern. Because myocardial contraction causes an increase in the sinusoidal frequency, while myocardial stretching causes a frequency decrease, the sinusoidal pattern is in fact related to the myocardial strain.

However, as the harmonic phase is a material property of the tagged tissue, the phase of a point in the tissue only changes in direct correspondence to the change in frequency of the sinusoid, which in turn reflects the underlying strain. Myocardial motion estimation can then be achieved by simply tracking the phase of the point of interest in a small region of interest (ROI) around it after phase wrapping correction. This technique results in automatic and fast analysis of tagged images.

The tags motion tracking in CINE images is achieved by searching for the point in a second image that has the same phase values as the tissue point in the first image. This process is repeated throughout the entire tag images sequence, i.e. during the entire cardiac cycle, which creates a path line for the selected point.

Lagrangian strain can be tracked by detecting the change in distance between two or more tracked points from cardiac cycle sequence of frames [69]. Because of the special geometry of the heart and its function, it is common to measure the strain in the radial and circumferential directions by placing a circular grid onto the LV wall. The points in the circular grid are tracked through the cardiac cycle and the circumferential strain is measured by the change in the distance between two neighboring points on a circumferential direction. The radial strain is measured by the change in the distance between neighboring points on the radial direction.

Eulerian strain calculation does not require the sequence of images from cardiac cycle, only one pair of harmonic phase images (horizontal and vertical in case of a grid tagging) are required, both corresponding to a single time frame in a cardiac cycle. After calculating the harmonic phases of these images in a given point, it is possible to compute a 2D strain tensor at that point. By repeating this process over all points in an image, and then to the whole sequence of images, it will be possible to detect all the variations in both circumferential and radial strains during the cardiac cycle.

The tracking of motion is done by tracking the deformation of tag points in image plane, which is two-dimensional. Figure 2.32 shows the apparent material point (q) corresponding to the orthogonal projection of the actual 3D material point location at end-diastole onto the image plane. It is also shown the position (y) of the material point after deformation. 2D motion does have a very precise relationship to the real 3D motion and therefore, all motion quantities derived from apparent motion, such as strain, can be related to the true 3D quantities in an equally rigorous way.

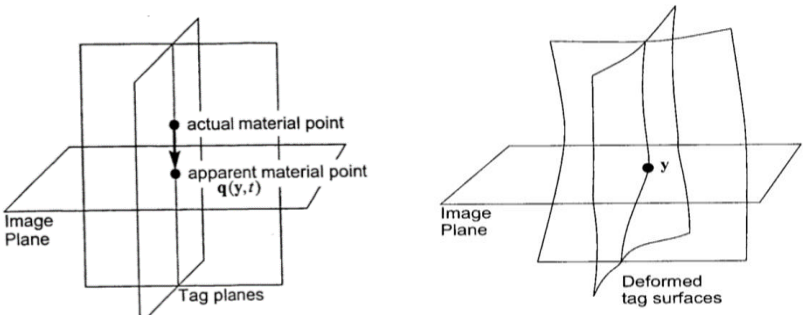

Reference frame at time t=0 Deformed frame at time t

Figure 2.32: Illustration of the actual and apparent (q) material points in initial reference frame at time t=0 (left) and in a deformed state (y) at time t (right). Adapted from [67].

Nevertheless, some efforts to improve HARP were to extend the strain analysis to 3D. In 2002, Haber et al. [70] proposed 3D myocardial motion analysis techniques based on extensions of 2D HARP. The authors derived a 3D finite element model for estimating myocardial 3D motion from multiple 2D tagged images. In 2005, the 3D HARP technique was proposed by Pan et al. [71] as a straightforward extension to HARP for fast and semiautomatic tracking of myocardial 3D motion. In this technique, a parallel set of SA grid-tagged images and a radial set of long axis images with horizontal tags are acquired to construct a 3D mesh around the LV. Motion tracking was automatically conducted using a 3D version of the constant harmonic phase also used in HARP. As a further step to minimize error accumulation during the transition from one timeframe to another, the phase of each material point was checked at each timeframe against its initial value. In the initial work, the 3D-HARP method compared well to other validated techniques and provided LV myocardial 3D motion analysis in about 10 minutes with very little human interaction [72].

3. Methods

3.1 Overview

The main goal of this project was to analyze the variation in time of radial strains during the cardiac cycle and along the LV sections, from sequences of MR images. Additionally, another aim was to evaluate whether these measured strains enable to distinguish healthy subjects from patients with LV desynchrony.

The noninvasive assessment of the cardiac function is of major interest for the diagnosis and the follow-up of cardiovascular pathologies. Whereas cardiac MRI (Figure 3.1) only allows to measure anatomical and functional parameters of myocardium, tagged cardiac MRI (Figure 3.2) makes it possible to evaluate the myocardial displacement and thus, enables the analysis of myocardium regional contraction (detection of potential contractible areas within the ischemic area). The acquisition protocol used by tagged MRI displays a deformable dark grid which follows the contraction of myocardium on the images of a temporal short axis (SA) sequence. The follow-up of this grid makes possible the evaluation of the intramyocardial displacement (Figure 3.3), because the grid deforms with the underlying tissue.

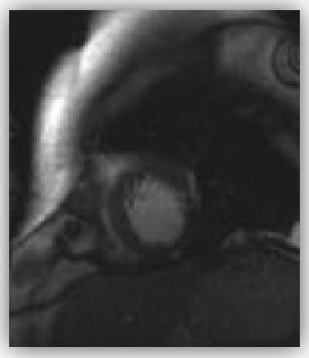

Figure 3.1: Example of a cardiac MRI image from the database

Figure 3.2: Example of a cardiac SPAMM MRI image from the database and the respective grid.

Figure 3.3: The follow-up of the left ventricle deformation grid in short axis MR images from end-diastole(ED) to end-systole (ES). From left to right, the grid deformation illustrates the contraction and displacement of the myocardium from ED to ES. [Images from this study]

3.2 Sample: healthy subjects and DCM patients

The database used in this thesis consists in a sample of MRI chest scans (DICOM format), which were analyzed in the Institute of Informatics, Robotics and Cybernetics from the Faculty of Electrical Engineering in Prague, Czech Republic. Images were acquired in 9 subjects (Table 3.1) aged 23-76 from Motol Hospital in Prague, who provided informed consent.

The data from each subject was acquired by clinicians and consisted of short-axis images of the heart during the cardiac cycle, that started in end-diastole and finished in end-systole. MR imaging was performed on a standard 1.5 T scanner Magnetom Avanto with software release Syngo MR B17 (by Siemens Healthcare headquarters, Siemens Healthcare GmbH, Erlangen Germany). The imaging frequency was 63.685 MHz, the flip angle was 14º, the field-of-view was 340x276.25 mm^2 and the acquisition matrix was 256x208 mm^2. The slices were 6 mm thick and there were only used SPAMM sequences. The tagging sequence was applied immediately after the detection of the R-wave on the ECG. Two sets of SPAMM pulses were performed sequentially to generate tags in two orthogonal directions to form a grid. Immediately following the tagging sequence, gradient-echo cine images were acquired during the entire cardiac cycle to follow the displacement of the tags. All the sets of MRI images have the previous mentioned acquisition parameters and the details for each set are specified in table 3.1.

Table 3.1: Data from the 9 subjects in this study

Subject	Gender (M/F)	Height (m)	Weight (kg)	Age (years)	Acquisition date	TR (ms)	TE (ms)	Slice Thickness (mm)	Group
1	M	1.78	90	59	06-10-14	34.68	4.2	6	DCM
2	M	1.84	95	72	16-03-16	26.01	4.2	6	DCM
3	M	1.85	118	68	08-12-14	26.01	4.2	6	DCM
4	F	1.74	78	48	26-01-16	26.01	4.2	6	DCM
5	F	1.5	65	69	14-03-16	34.68	4.2	6	Healthy
6	M	1.74	71	76	26-11-14	26.01	4.2	6	DCM
7	F	1.7	68	23	23-02-15	34.68	4.2	6	Healthy
8	F	1.69	75	41	04-05-15	43.35	4.2	6	Healthy
9	F	1.73	70	50	06-12-14	26.01	4.2	6	DCM

From the 9 subjects, the 3 grouped as healthy are controls and don't have any historical of heart or cardiovascular disease.

All subjects grouped as DCM in the table have the diagnosis of heart failure due to dilated cardiomyopathy and signs of electrical dyssynchrony. This dyssynchrony was assessed based on the duration and morphology of the QRS complex. They had MRI before CRT implantation and there was no previous heart intervention or surgery related to this diagnosis.

3.3 Strain analysis: step by step

The analysis of tagged MR images in this dissertation consisted of three steps. At first, the endocardial and epicardial contours of the left ventricle (LV) were defined either manually or with semi-automated algorithms. Secondly, the tag lines were segmented in every image of the sequence. In most cases, the line intercessions were used as feature points during the tracking. Lastly, the strain analysis was done by the quantification of the line intersections displacements. The first and second steps were only performed with MATLAB software, while the third step was performed on both MATLAB and Microsoft Excel.

1st Step – FOV definition and Left Ventricle borders defined

In the first action when running the program, the user is prompt to choose the data folder

containing the DICOM images from the patient to analyze. The first frame of the folder is opened and the user needs to crop the MRI image, i.e. select a sub-area (ROI) containing the LV. The crop is semiautomatic as it consists on the automatic detection of the LV but the size of the image crop is defined manually. A manual crop consists of using the *imcrop* tool in *Matlab*, in which the user designs a rectangle shape mask containing the LV in the center. After the first click, the rectangle begins to get shape as the cursor moves and gets its final shape after the second click in the desired location. Although the heart's position may vary between scans, the LV was found closed to the center of the FOV in all the frames, so it was possible to semi-automatically select the ROI containing the LV in the center in all images and in all temporal frames.
After that, the LV borders were approximately represented by circular shapes in all frames, which defined the endocardial and epicardial limits of the myocardial walls (see Figure 3.4). This eliminates the necessity to define the LV contours in every frame of the image sequence, which is a difficult task. The LV contours are then defined only in the first frame.

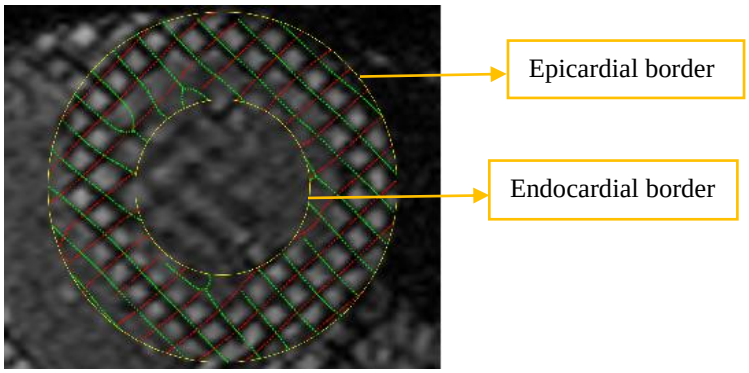

Figure 3.4: Short-axis image with the endocardial and epicardial borders of the LV wall in yellow. [Image from this study]

2nd Step – Tagging detection and tracking

The aim is to obtain the changes of LV strain in time, i.e. through the consecutive cardiac MRI scans of the patient.

To do that, the first thing needed is to apply a 2D Fourier Transform to each image. As the images are composed by two sets of perpendicular tagging sequences forming a grid, the respective FT will have a pattern of peaks. The FT of a tagged image consists of the central peak (DC component) and the harmonic peaks. The amplitude spectrum of a tagged image that contains the frequency peaks is shown in Figure 3.5.

The two sets of orthogonal tagging patterns of the image originate a central peak and four first harmonic peaks: two peaks in 45º and 225º due to one orthogonal direction of the tagging and other two in 135º and 315º due to the other orthogonal direction. The 45º and 225º peaks hold the information about the parallel stripes that vary according to the 45º direction and the 135º and 315º peaks hold the information about the parallel stripes that vary in the 135º direction. The harmonic spectral peaks around the DC component are antisymmetric and thus can be easily calculated by simply knowing the location of one of the first harmonic peaks.

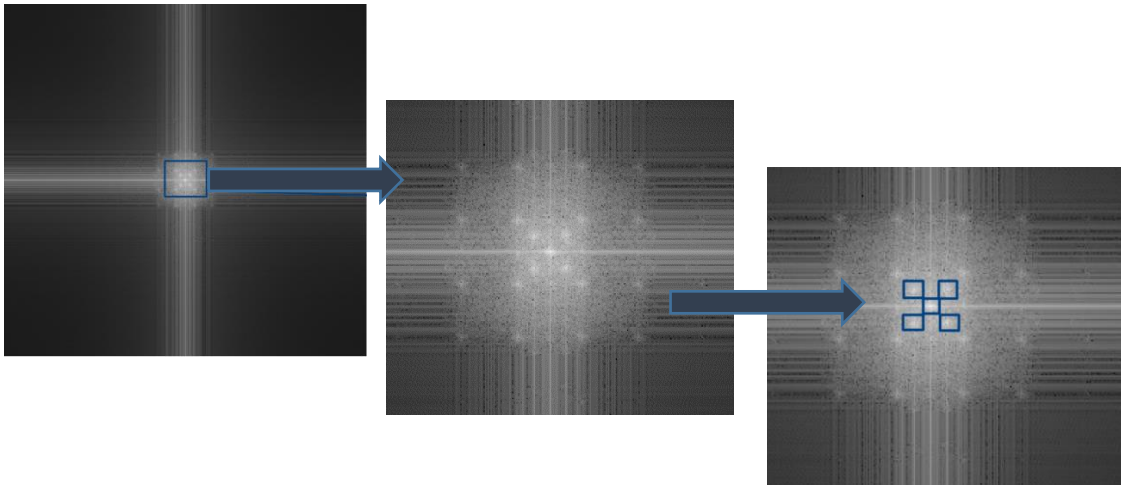

Figure 3.5: Fourier Transform of the SPAMM MRI image represented in Figure 3.2 (left) and a closer visualization of the peaks (image in the middle). The two sets of orthogonal tagging patterns of the image originate a central peak and four harmonic peaks: two peaks in 45º and 225º due to one orthogonal direction and other two in 135º and 315º due to the other orthogonal direction of tagging (at right). [Images from this study]

In the k-space of a harmonic image, most of the spectral energy is concentrated in the spectral peaks. In order to obtain the information of the grid and tags, all the five peaks must be filtered by a band-pass filter and the bandwidth of the filter must be chosen carefully to minimize the influence of other spectral peaks and maximize the contribution of the desired peak to extract the tag deformation and eliminate the noise. As previously mentioned, myocardial tissue stretching will cause a decrease in the magnitude of the central peak and myocardial tissue contraction will cause an increase in the central frequency. The size and position of the bandpass filter needed to be properly positioned in order to capture the spectral energy, which also changes during the cardiac cycle according to the heart strain. The bandpass filter for the central peak was designed to be a circular shaped mask centered in the position of the central peak (i.e. maximum frequency in the image k-space) and it had a radius equal to approximately 50% of the maximum frequency (Figure 3.6). By finding the second major spectral frequency peaks, it was possible to find the location of the harmonic peaks at 45º and 135º. Because the 45º and 225º peak positions are symmetric relatively to the central peak, it was easy to calculate the position of the 225º peak from the 45º one. Additionally, by finding the location of the 135º peak, the 315º peak location is respectively discovered. A similar filter of the central peak was designed for these four peaks, and the corresponding inverse FT image was obtained. This image was very similar to the original image before FT application, but the FT application improved the grid detection.

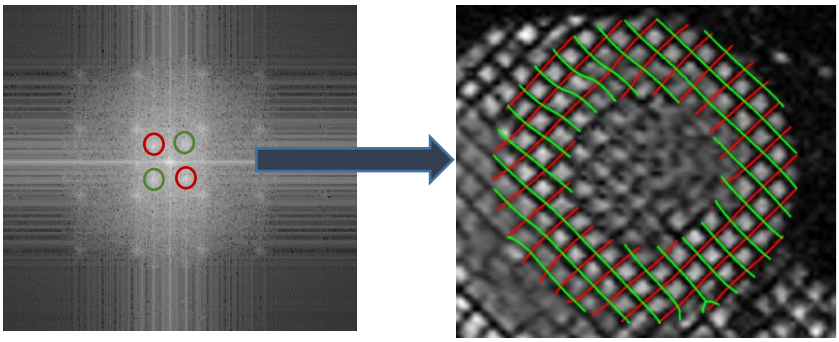

Figure 3.6: At left, the circular filters to filter the four harmonic peaks at 45º and 225º (in green) and at 135º and 315º (in red). At right, the corresponding grid obtained by the two sets of tagging lines are represented in green and red, respectively.

The commonly used method designed for edge detection in horizontal and vertical directions is the Prewitt filter. However, as the grid is composed by 2 sets of diagonal lines, there was a need to adapt the Prewitt filter to detect each set of lines (equations 3.1 and 3.2). Equation 3.1 corresponds to the 45º diagonal filter and equation 3.2 corresponds to the 135º diagonal filter.

$$\text{Prewitt}45^{o} = \begin{bmatrix} 1 & 1 & 0 \\ -1 & 0 & 1 \\ 0 & -1 & -1 \end{bmatrix} \tag{3.1}$$

$$\text{Prewitt}135^{o} = \begin{bmatrix} 0 & 1 & 1 \\ -1 & 0 & 1 \\ -1 & -1 & 0 \end{bmatrix} \tag{3.2}$$

The Prewitt operator is a gradient method, which detects the edges (e.g. LV wall borders) by finding the maximum and minimum of the first derivatives in the image, as the image is a continuous derivative of intensity points [73]. The Prewitt filter is then a discrete differentiation operator, which computes the gradient of the image intensity function, by convolving the image with an integer valued filter. At each point in the image, the result of the Prewitt operator convolution leads to the diagonal edge detection, as shown in figure 3.6.

After some morphological operations as *skel*, in which the pixels on the boundaries of the lines corresponding to edges detected are removed without breaking the lines apart, and *spur*, which removes end points of lines without changing the line integrity, it is possible to detect the tags. The tags are detected by the intersection of both sets of diagonal edges detected and are represent as yellow circles in figure 3.7.

The wall deformation can be analyzed due to the LV wall tags detection. By applying this method to all of the consecutive images from each patient, it is possible obtain the variation of the LV tags location and predict the LV strains during the entire cardiac cycle.

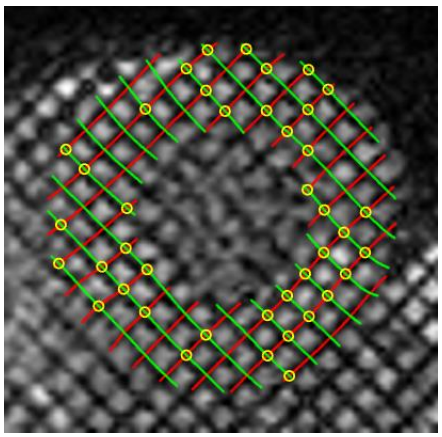

Figure 3.7: Tags detected by the intersection of the two sets of diagonal lines (45º diagonals denoted in red and 135º diagonals in green) represented in yellow circles.

The basic idea behind all tagging analysis techniques is to track adjacent tag intersection points and measure relative increases or decreases between them from one-time frame to another to calculate strain. Various strain components are measured throughout the cardiac cycle: circumferential and radial strains are measured from short axis images, while longitudinal strain is measured from long-axis images. In this thesis, only short axis images were used, so that it was possible to calculate LV circumferential and radial strains. Radial strain is calculated by the tags

displacement within the radius of the LV wall in a short-axis view. A positive strain corresponds to an increase in radius length, i.e. to a LV wall thickening. Circumferential strain corresponds to the ratio of the LV wall circumference change to the original circumference. Therefore, negative circumferential strain corresponds to LV wall shortening.

For deformation analysis, the reference configuration is identified as the non-deformed configuration and corresponds to the first time frame within the patient folder and also to the end-diastolic frame. This time frame is the starting point for tracking, where the two orthogonal sets of tag lines represent a non-deformed grid and have the highest contrast. Similarly, to the Lagrangian strain, the strains in this thesis are analyzed by calculating the displacement of the tags within the remaining frames through the cardiac cycle relatively to the tags in the first frame.

3rd Step - Myocardial segmentation and analysis

In order to study the local deformations in LV, there is a need to divide the LV in sections and segments to calculate the strain within these regions and compare them with remaining MRI frames.

The LV muscle and cavity can be divided into a variable number of segments. Based on autopsy data, the American Heart Association [74] recommended a division in 17 segments for the regional analysis of LV deformation. The cardiac segments can be arranged as a polar plot with six basal segments, six mid-cavity segments, four apical segments, and the apex in the center. This division makes it easier to compare the LV strain in the different parts of the LV or between heathy subjects and patients. The numbering and identification of the cardiac segments is illustrated in Figure 3.8.

The left ventricle is firstly divided into three parts perpendicular to the long axis of the heart (Figure 3.8 – at left), which are the basal, mid-cavity, and apical sections.

The basal section is divided into six segments of 60° each (Figure 3.8- yellow section). The segment names along the circle are basal anterior, basal anteroseptal, basal inferoseptal, basal inferior, basal inferolateral, and basal anterolateral. The septum is identified by the right ventricular attachment to the LV wall.

Similarly, the mid-cavity part is divided into six 60° segments (Figure 3.8- pink section), which are the mid anterior, mid anteroseptal, mid inferoseptal, mid inferior, mid inferolateral, and mid anterolateral segments.

Only four segments of 90° each are used for the apical part (Figure 3.8- blue section) because of the myocardial narrowing. The segment names are apical anterior, apical septal, apical inferior, and apical lateral. The extreme limit of LV, where there is no longer cavity present, is named apex (Figure 3.8- white section).

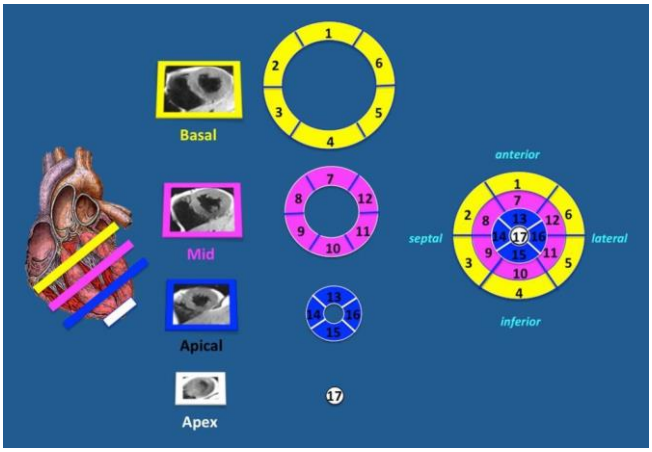

Figure 3.8: Left Ventricular segments. In the basal section, the segment 1 corresponds to the basal anterior part of LV, the 2nd and third segments correspond to the basal anteroseptal and inferoseptal locations, which are the locations near the septum and right ventricle. The segment 4 is the basal inferior, and the segments 5 and 6 correspond to basal inferolateral and basal anterolateral, respectively. Segments 7 to 12 have identical designations to segments 1 to 6. However, instead of being located in the LV base, the segments are in the mid section, and so are named mid anteroseptal (segment 2) and mid inferoseptal (segment 3). In the apical part, there was a division on 4 segments, from 13 to 16. These for segments are apical anterior, apical septal, apical inferior, and apical lateral. The apex (segment 17) is the limit of of the ventricle where there is no longer cavity present. Adapted from [75]

This thesis adapted the segment model with two changes: the mid and apical segments were also numbered from 1 to 6 segments, according to the basal orientation (Figure 3.9). For example, the anterior segment corresponds to the number 1 for all the sections: base, mid and apical. Therefor the number 1 is the basal anterior segment in basal section, mid anterior segment in mid section and apical anterior segment in apical section. This approach was followed for the remaining segments (Table 3.2). That way it is visually possible to merge all the segments separated by sections in one only graphic, as seen in results section.

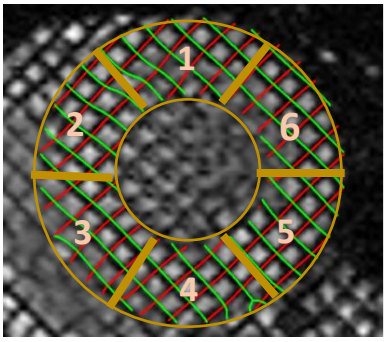

Figure 3.9: Segments numbered from 1 to 6 in all the LV sections (Base, Mid, Apical).

Table 3.2: LV segments numbered by each section (base, mid, apical).

Basal Segments		Mid-cavity Segments		Apical Segments	
1.	basal anterior	1.	mid anterior	1.	apical anterior
2.	basal anteroseptal	2.	mid anteroseptal	2.	apical anteroseptal
3.	basal inferoseptal	3.	mid inferoseptal	3.	apical inferoseptal
4.	basal inferior	4.	mid inferior	4.	apical inferior
5.	basal inferolateral	5.	mid inferolateral	5.	apical inferolateral
6.	basal anterolateral	6.	mid anterolateral	6.	apical anterolateral

After detecting the tag lines to fit the stripes created by SPAMM, from frame to frame, it was possible to analyze the cardiac strains by calculating the tags' displacement through the cardiac cycle comparatively to the tags in the first frame of the set of frames. The displacement values related to circumferential and radial strains were exported to an excel file and were used for studying the differences between LV segments and for the classification of normal or diseased heart function, as will be shown in the results section.

4. Results

4.1 Visualize the grid deformation

At first it is required to select the Region Of Interest (ROI), which should include the left ventricle in the MR image (Figure 4.1). The MR image is the first frame of the subject folder and corresponds to end-diastole, i.e. the non-deformed state of SPAMM grid.

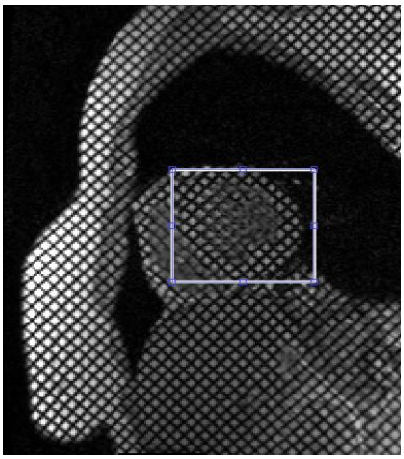

Figure 4.1: Region of Interest selection

The grid tracking is visualized in the next sequences of images within figure 4.2.

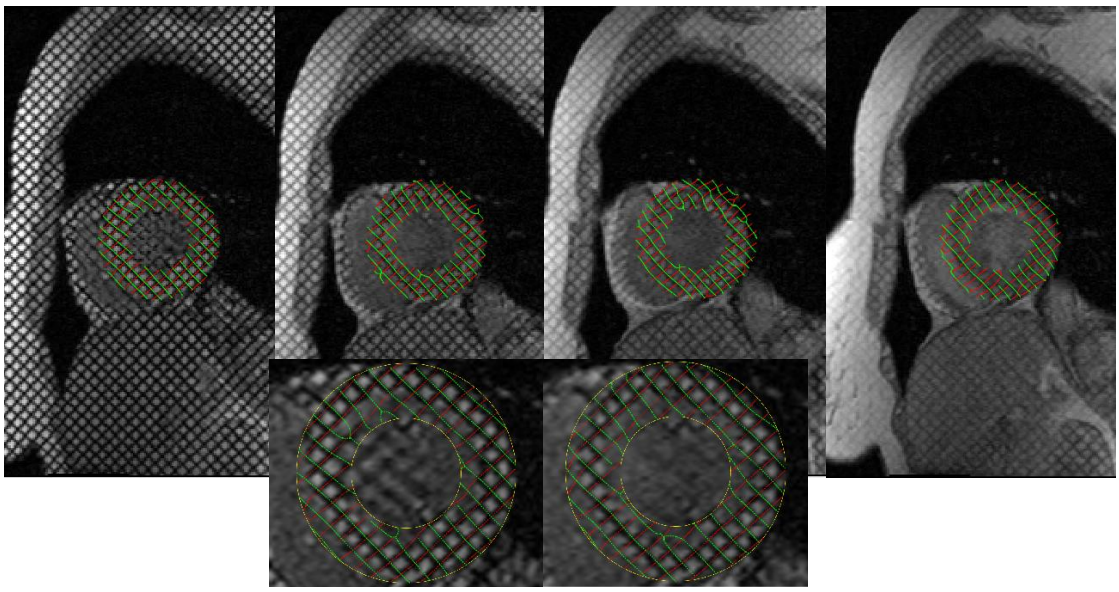

Figure 4.2: Grid tracking visualization of a dilated cardiomyopathy patient's left ventricle during cardiac cycle, from end-diastole (ED) to end-systole (ES) – left to right of the figure. The end-diastole (ED) to end-systole (ES) zoomed images are represented below, in the middle of the figure.

In this figure, the first frame corresponds to the end diastole, which is the non-deformed state and the start point for the grid tracking. From the two zoomed images in the middle and below within the figure 4.2, it is possible to visualize the endocardial and epicardial borders in yellow. These borders are automatically defined in all the frames of the images sequence, which increases the efficiency of this method, as there is no need to define the LV contours in every frame of the set. Additionally, it is confirmed that the tracking method worked properly, as the tags from SPAMM MRI images were correctly detected and replicated by the green and red diagonal lines. The yellow circles are the intersections between the two sets of lines and are the tag points used to calculate the deformations.

Because there is a need to compare the strains between DCM patients and healthy subjects, two examples of the strain calculation method applied to a patient and a healthy subject are shown next in section 4.1.1 and 4.1.2, respectively. The patient in the example is the first one on the table 3.1 and the healthy subject is the fifth one. The subjects for each example were randomly chosen from the table.

As the LV is divided in three sections (basal, mid and apical), a sequence of the grid tracking is presented within the three sections of the LV, for each of the two subjects. Moreover, as the LV sections are divided in segments, as explained in section 3.3 of this thesis, the radial strains were also calculated for all the segments by each LV section, and are represented in graphics. The radial strain is calculated during systole, from the different frames relative to the first frame (end-diastole).

4.1.1 DCM patient - Subject 1 (Gender: M, Age: 59 years)

This section analyses the strains of a DCM patient during the cardiac cycle by showing the sequence of grid tracking and deformation along the cycle, i.e. from end diastole to end systole states, for each LV section (basal, mid and apical). Additionally, the radial strain values were calculated for all the systole frames of the patient and the average value of the radial strain was presented for each segment within each LV section.

Basal section

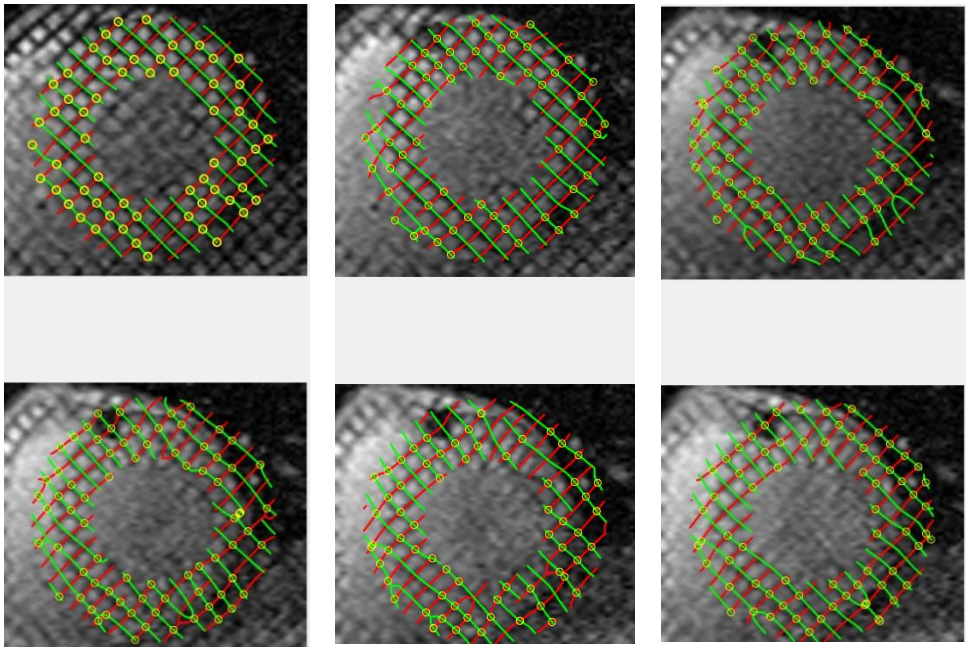

Figure 4.3: Sequence of a DCM patient's LV base strain during cardiac cycle. The red and green sets of lines represent the SPAMM grid and the yellow circles are the intersections detected between the two sets.

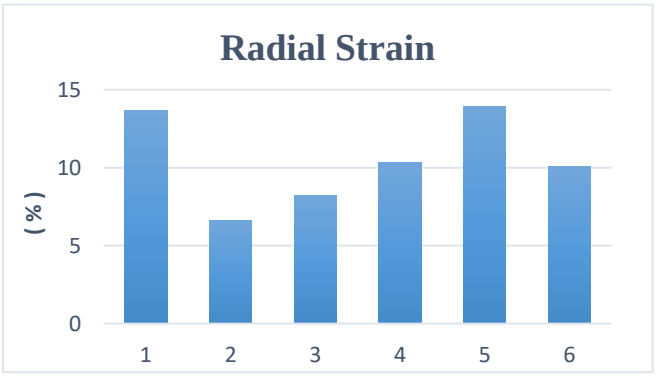

Figure 4.4: Average LV radial strain of a DCM patient (subject 1 from table 3.1) by each segment within LV basal section. The radial strain is calculated during systole, from the different frames relative to the first frame (end-diastole). The numbers 1 to 6 correspond to each one of the segments, as described in figure 3.9.

Mid section

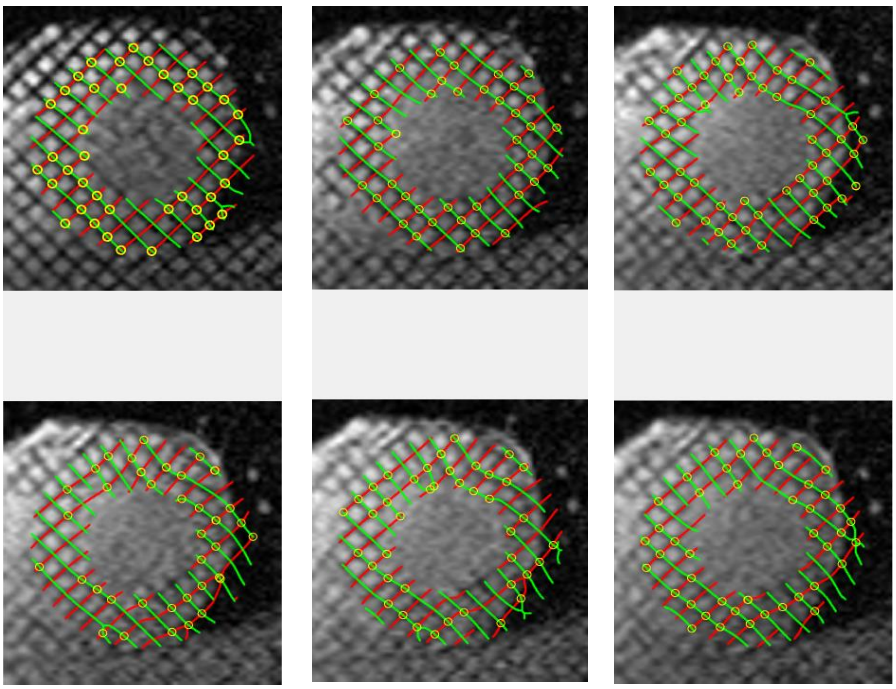

Figure 4.5: Sequence of a DCM patient's LV mid section strain during cardiac cycle. The red and green sets of lines represent the SPAMM grid and the yellow circles are the intersections detected between the two sets.

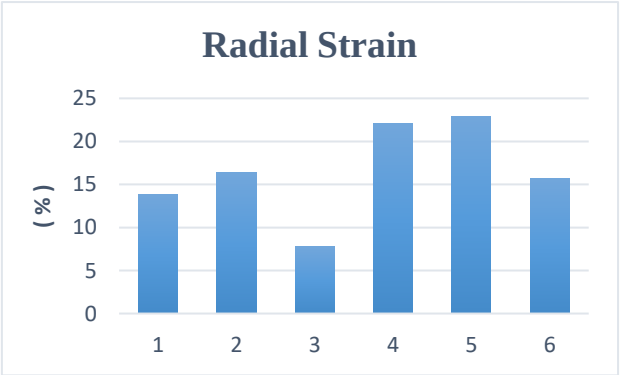

Figure 4.6: Average LV radial strain of a DCM patient (subject 1 from table 3.1) by each segment within LV mid section. The radial strain is calculated during systole, from the different frames relative to the first frame (end-diastole). The numbers 1 to 6 correspond to each one of the segments, as described in figure 3.9.

Apical Section

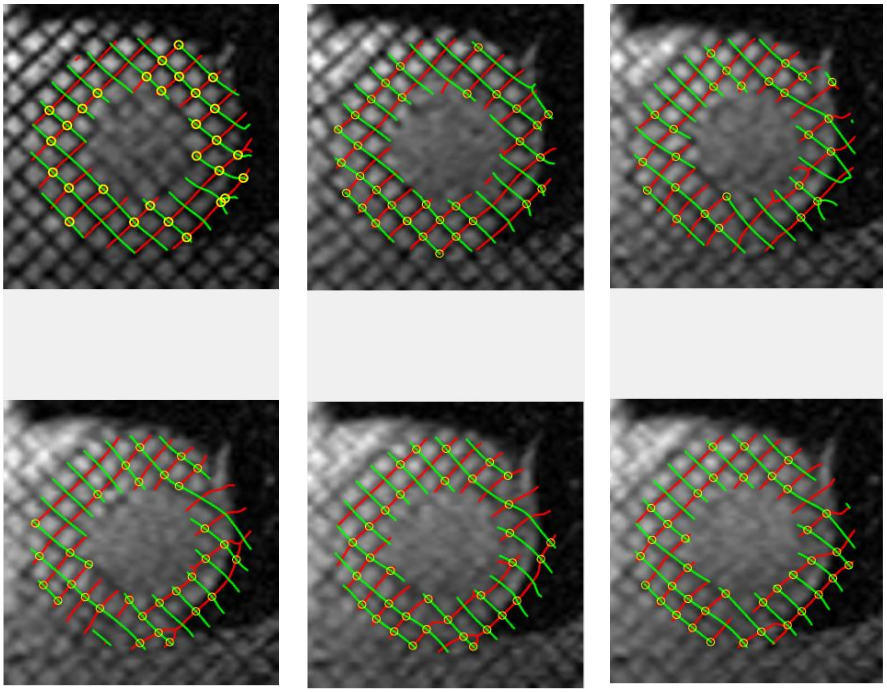

Figure 4.7: Sequence of a DCM patient's LV apical section strain during cardiac cycle. The red and green sets of lines represent the SPAMM grid and the yellow circles are the intersections detected between the two sets.

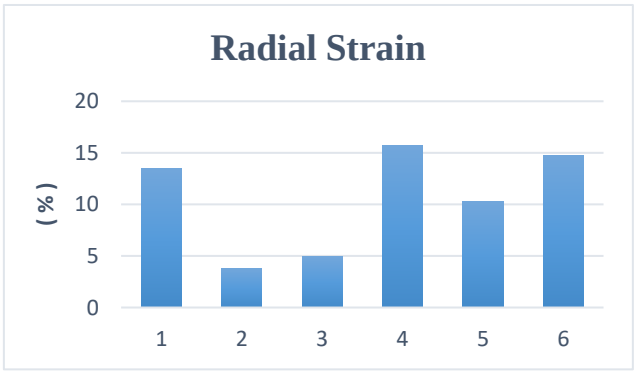

Figure 4.8: Average LV radial strain of a DCM patient (subject 1 from table 3.1) by each segment within LV apical section. The radial strain is calculated during systole, from the different frames relative to the first frame (end-diastole). The numbers 1 to 6 correspond to each one of the segments, as described in figure 3.9.

4.1.2 Healthy subject - Subject 5 (Gender: F, Age: 69 years)

This section analyses the strains of a healthy subject during the cardiac cycle by showing the sequence of grid tracking and deformation along the cycle, i.e. from end diastole to end systole states, for each LV section (basal, mid and apical). Additionally, the radial strain values were calculated for all the systole frames of the subject and the average value of the radial strain was presented for each segment within each LV section.

Basal section

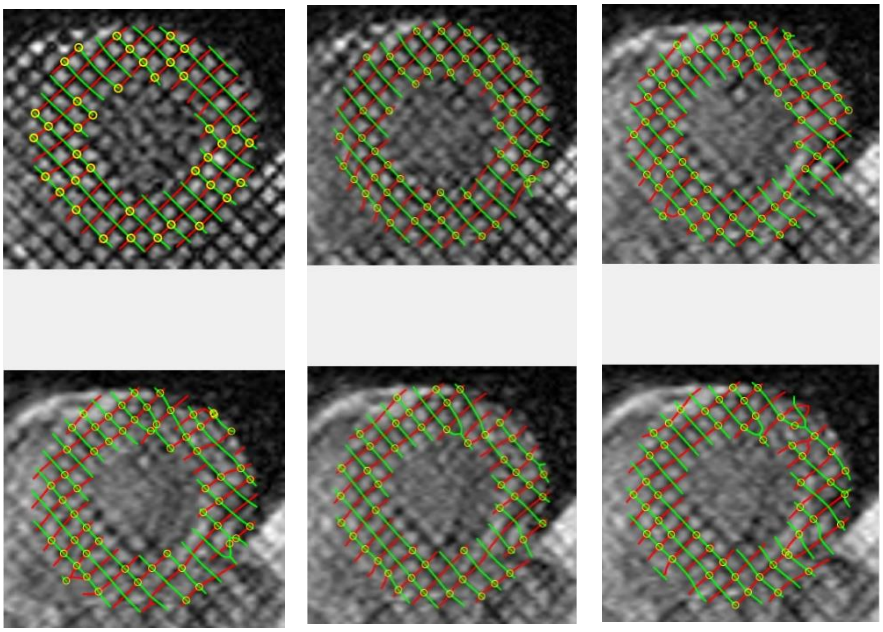

Figure 4.9: Sequence of a healthy subject's LV base strain during cardiac cycle. The red and green sets of lines represent the SPAMM grid and the yellow circles are the intersections detected between the two sets.

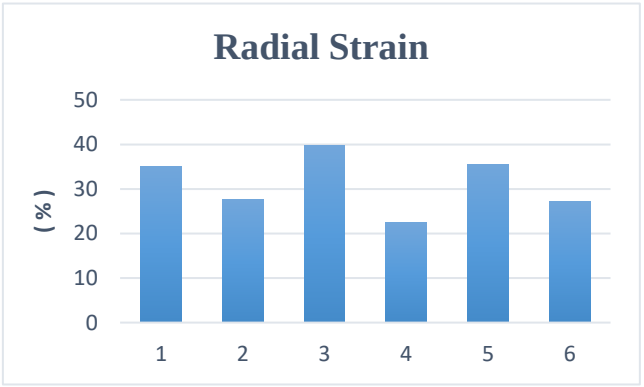

Figure 4.10: Average LV radial strain of a healthy subject (subject 5 from table 3.1) by each segment within LV basal section. The radial strain is calculated during systole, from the different frames relative to the first frame (end-diastole). The numbers 1 to 6 correspond to each one of the segments, as described in figure 3.9.

Mid section

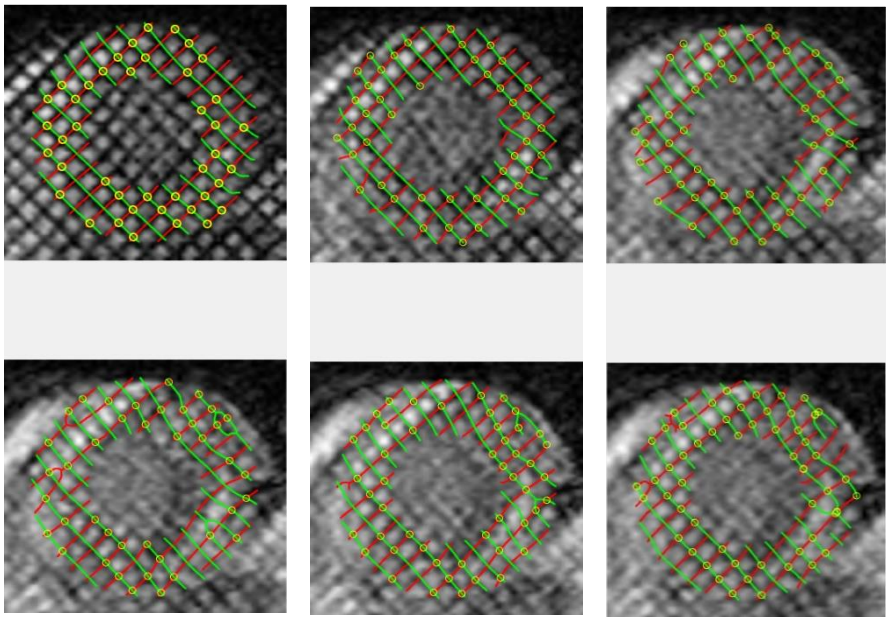

Figure 4.11: Sequence of a healthy subject's LV mid section strain during cardiac cycle. The red and green sets of lines represent the SPAMM grid and the yellow circles are the intersections detected between the two sets.

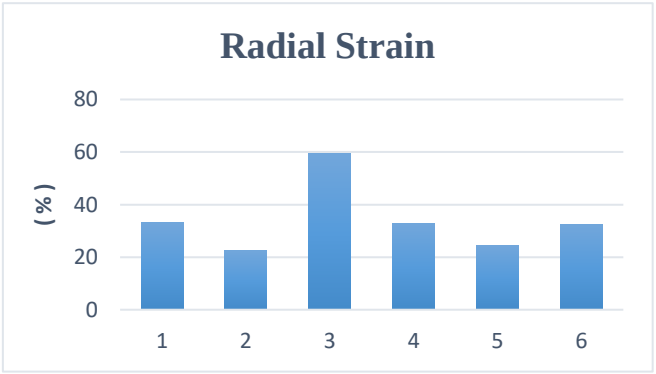

Figure 4.12: Average LV radial strain of a healthy subject (subject 5 from table 3.1) by each segment within LV mid section. The radial strain is calculated during systole, from the different frames relative to the first frame (end-diastole). The numbers 1 to 6 correspond to each one of the segments, as described in figure 3.9.

Apical section

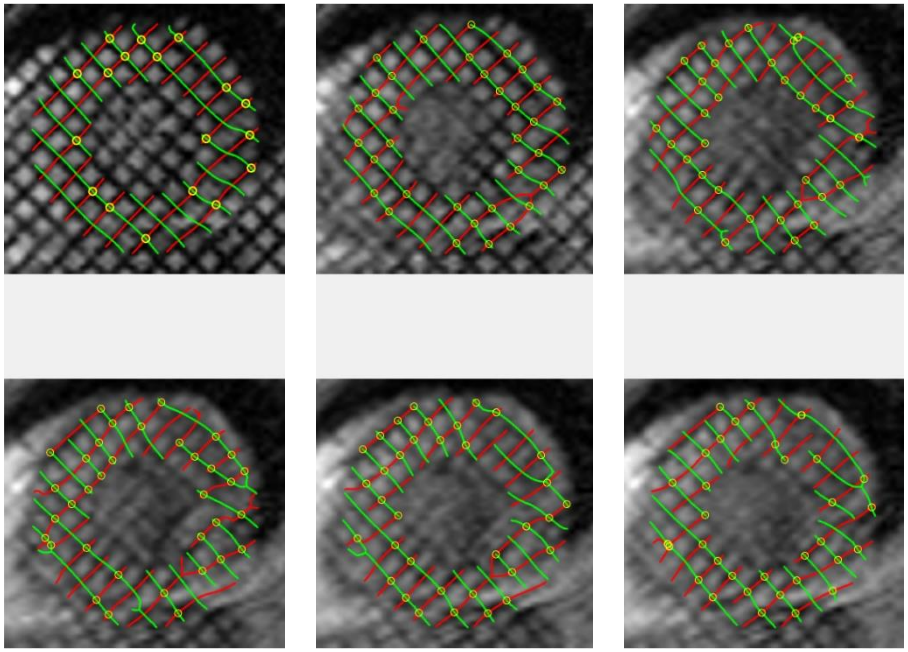

Figure 4.13: Sequence of a healthy subject's LV apical section strain during cardiac cycle. The red and green sets of lines represent the SPAMM grid and the yellow circles are the intersections detected between the two sets.

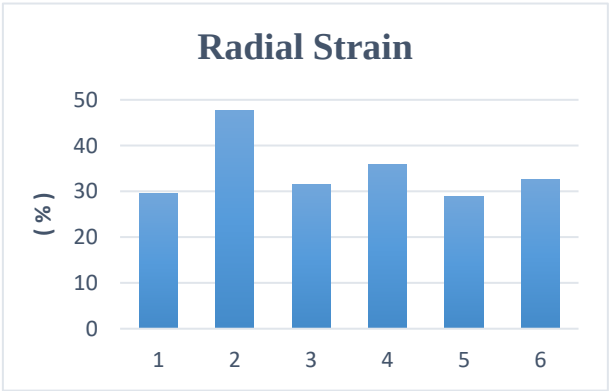

Figure 4.14: Average LV radial strain of a healthy subject (subject 5 from table 3.1) by each segment within LV apical section. The radial strain is calculated during systole, from the different frames relative to the first frame (end-diastole). The numbers 1 to 6 correspond to each one of the segments, as described in figure 3.9.

4.2 Radial strain: Base, Middle and Apical

This section shows the average radial strains of all DCM patients (figure 4.15) and healthy subjects (figure 4.16) during systole by each LV section (basal, mid and apical) and the respective segments. The average strain was calculated from the different frames relatively to the first frame (end-diastole).

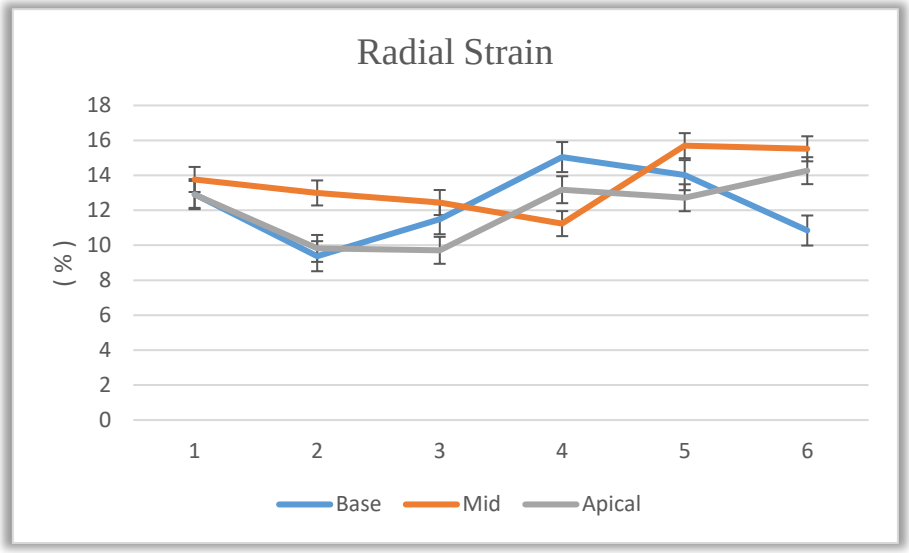

Figure 4.15: Average LV radial strain of all DCM patients by LV section and respective segments. The radial strain is calculated during systole, from the different frames relative to the first frame (end-diastole). The numbers 1 to 6 correspond to each one of the segments, as described in figure 3.9.

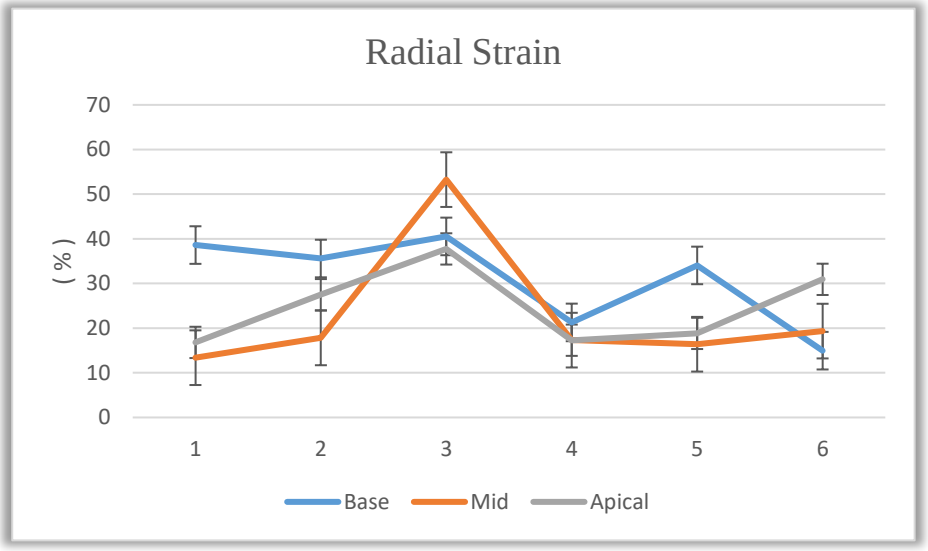

Figure 4.16: Average LV radial strain of the healthy subjects by LV section and respective segments. The radial strain is calculated during systole, from the different frames relative to the first frame (end-diastole). The numbers 1 to 6 correspond to each one of the segments, as described in figure 3.9.

4.3 Circumferential strain: Base, Middle and Apical

This section shows the average circumferential strains of all DCM patients (figure 4.17) and healthy subjects (figure 4.18) during systole by each LV section (basal, mid and apical). The average strain was calculated from the different frames relatively to the first frame (end-diastole). As the circumferential strain is a measure of the variation of the tags displacement within the LV in the circumferential direction, the deformation was calculated as an average by each LV section.

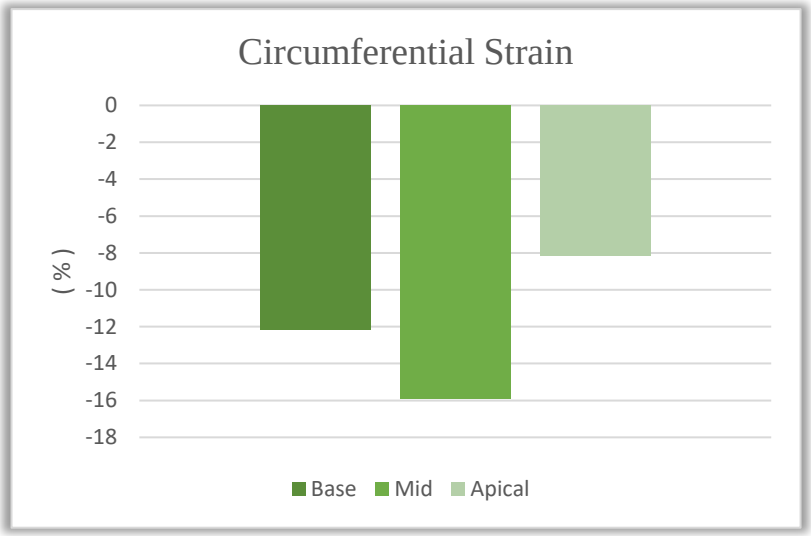

Figure 4.17: Average LV circumferential strain of the DCM patients by LV section. The circumferential strain is calculated during systole, from the different frames relative to the first frame (end-diastole).

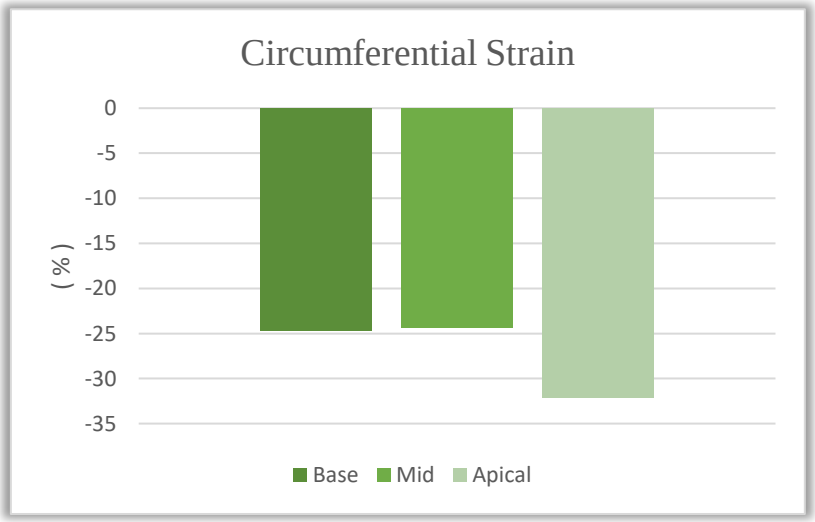

Figure 4.18: Average LV circumferential strain of the healthy subjects by LV section. The circumferential strain is calculated during systole, from the different frames relative to the first frame (end-diastole).

4.4 Healthy subjects and DCM patients

This section shows the comparison between the two sets of DCM patients and healthy subjects respectively to the radial (figure 4.19) and circumferential (figure 4.20) strains. The radial strain values are an average of all the LV sections but compared between each of the LV segments (1,2,3,4,5 and 6). Additionally, the circumferential strains were calculated from the different frames relatively to the first frame (end-diastole). As the circumferential strain is a measure of the variation of the tags displacement within the LV in the circumferential direction, the deformation was calculated as an average by each LV section.

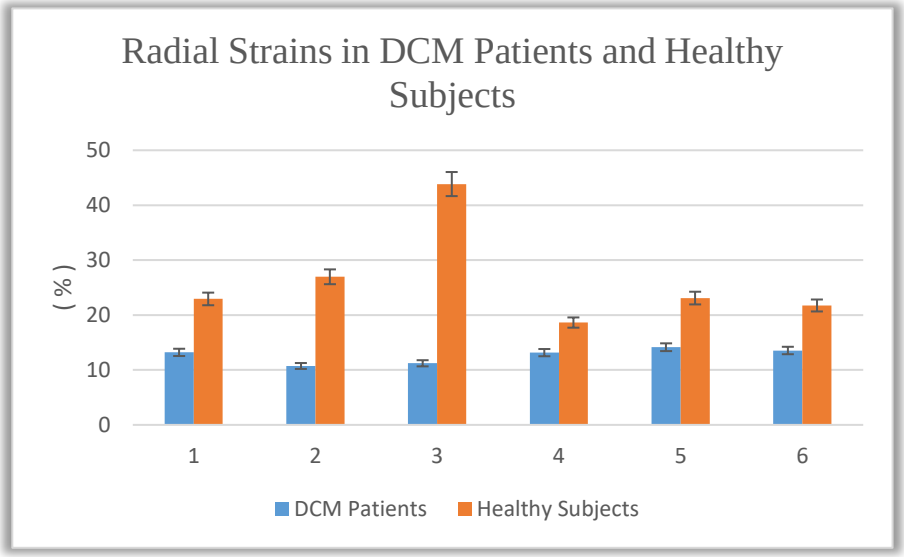

Figure 4.19: Average LV radial strains comparison between DCM patients and healthy subjects by LV segments. The radial strain is calculated during systole, from the different frames relative to the first frame (end-diastole). The numbers 1 to 6 correspond to each one of the segments, as described in figure 3.9.

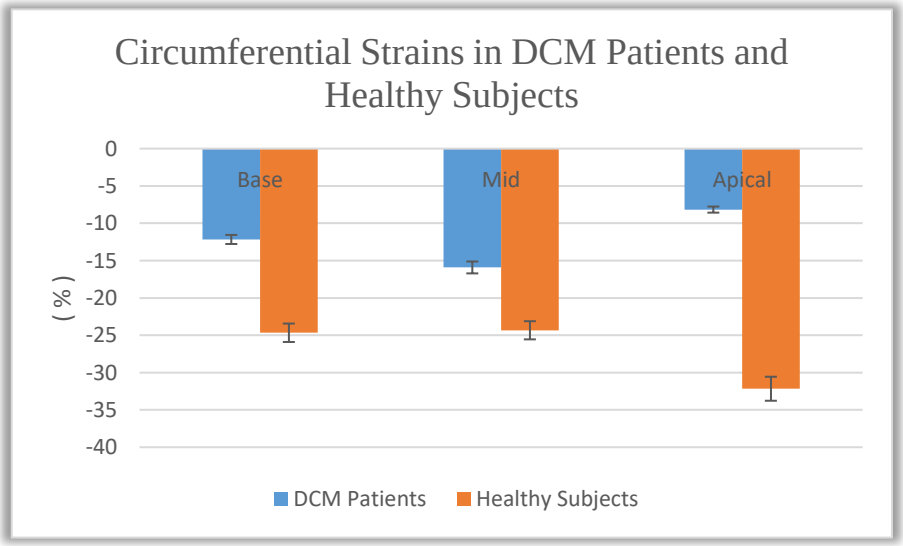

Figure 4.20: Average LV circumferential strains comparison between DCM patients and healthy subjects by LV section. The circumferential strain is calculated during systole, from the different frames relative to the first frame (end-diastole).

In order to have an analysis on the significance of the differences between the strains in healthy subjects and DCM patients, the Mann-Whitney U-Test was applied to both radial and circumferential strain values over the two sets of subjects in this study. Mann-Whitney U-Test is a non-parametric test used for comparing the median between two different groups, which have independent observations. The results of the test shown that there were significant differences ($p<0.05$) between the groups for radial strains and circumferential strains. In the radial strains comparison test, the p-value was 0.013, and in the test for circumferential strain, the p-value was .027, As both p-values are inferior to the significance level 0.05, then there is a significant difference between the medians of the radial and circumferential strains between DCM patients and healthy subjects.

4.5 Average Strain by Gender (Male/ Female)

In this section, the gender effect in DCM patients radial strains is analyzed by each LV section (basal, mid and apical).

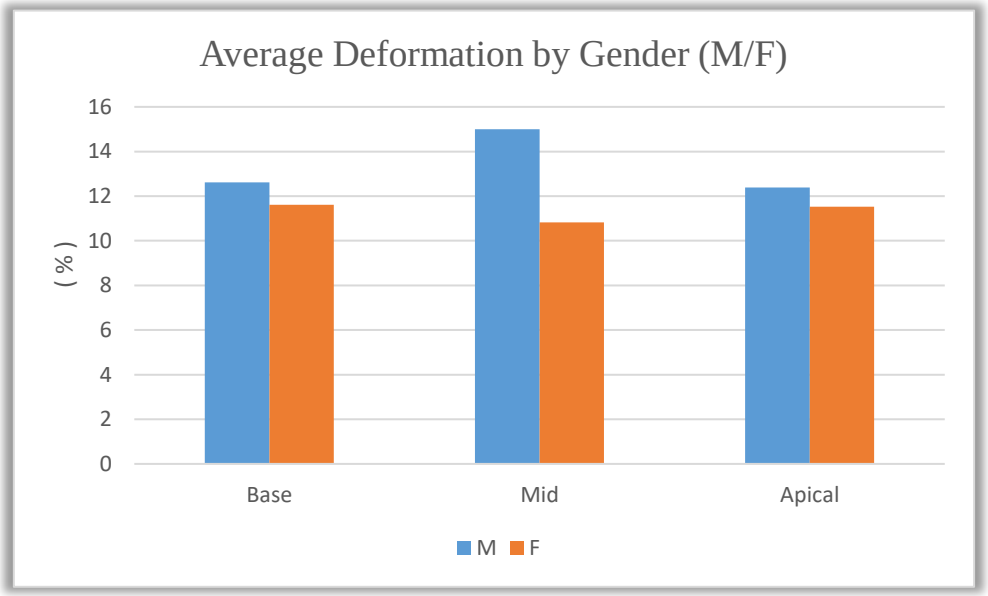

Figure 4.21: Average LV radial strains comparison between males and females by LV section in DCM patients. The radial strain is calculated during systole, from the different frames relative to the first frame (end-diastole).

5. Discussion and Future Work

The proposed thesis intended to assess the left ventricle (LV) radial strain by automatically detecting LV tags and tracking those during cardiac cycle. By analyzing the heart strains from healthy subjects and patients with DCM, it was possible to compare both patterns of cardiac deformation within the cardiac cycle in order to analyze the differences between them.

Initially, after studying how the LV wall was positioned in all the MRI scans, the LV wall borders were approximated by circumferences corresponding to the endocardium and epicardium edges. However, the edge detection of endocardium, myocardium and epicardium could also be performed by an edge detection method. Laplacian of Gaussian filter and Hough Transform are examples of these methods. Both methods were studied for this thesis, however there were many edges and circles detected in both methods, as the input data was a set of SPAMM images, and therefore had a superimposed grid that makes it difficult to detect the LV wall. These examples of an automatic way to perform the edge detection are harder to implement but would be more efficient, so that it can be a future work. Additionally, the ROI containing the LV is set by the user, so this task could also be automated by the detection of the LV in the images.

In this thesis, the tagging analysis tracked adjacent tag intersection points and measured relative increases or decreases between them, from one time frame to another to calculate strain. As only short axis images were used, it was possible to calculate LV circumferential and radial strains. Furthermore, strain rate could be obtained by differentiating myocardial strain with respect to time, which gives useful information about the degree of heart dysfunction, e.g. evaluating myocardial relaxation rate in diastolic dysfunction. Occasionally, myocardial twist angle may be obtained by measuring circumferential strain difference between parallel short axis slices.

From Figure 4.2, it is possible to conclude that the tagging process was successful, as the tag lines and respective tags intersections created by SPAMM deformed according to the expected heart muscle deformation and were precisely detected and tracked for wall motion studies.

Positive strain values describe thickening and negative values describe shortening of a given myocardial segment related to its original length. During myocardial contraction, as the wall shortens, it also thickens and thus, the radial strain is positive (myocardial thickening) and circumferential strain is negative (myocardial shortening).

By analyzing the healthy subjects' radial strains (Figure 4.16), the average radial strain range, by LV section (basal, mid and apical) and respective segments (1,2,3,4,5, and 6), was from 18.63 % to 43.84 %, while in DCM patients (Figure 4.15) it was from 10.73 % to 14.14 %. A comparison between the radial strains during systole in both sets of subjects (Figure 4.19) shown a significant difference between them ($p<0.05$). The results of this thesis support the results of previous studies [76-79] done with DCM and healthy subjects, as the ranges of deformations are similar in both sets of subjects. So that, this thesis confirms that DCM patients have lower strain values than healthy subjects, as DCM is characterized by a decrease in heart muscle strain during cardiac cycle.

By comparing the several segments in the different sections of the heart (Figures 4.15 and 4.16), it was also observed that in DCM patients, the minimum deformation was on the inferolateral segment of the base (segment 5), while the maximum was on the anteroseptal segment of the middle section (segment 2). However, in healthy subjects, the minimum deformation was on the anterior segment (segment 1) and the maximum was on the inferoseptal

segment (segment 3), both in the middle section of the left ventricle. While in DCM patients, the strains are similar and do not vary much along the segments, the strains further diverge in healthy subjects, in which the 3rd segment (inferoseptal) has a major deformation peak. This was also observes in the previous study regarding to the myocardial strains of DCM patients [77].

Regarding the circumferential strains, it was observed that in healthy subjects (Figures 4.18 and 4.20), the average circumferential strain range was from -32.17 % to -24.33 %, while in DCM patients (Figures 4.17 and 4.20), it was from -15.92 % to -8.17 %. In spite of the circumferential strain values being negative, the absolute value of the strain is the one that counts for the strain analysis. The negative value only means that there was a LV wall shortening and this is in conformity with the correct behavior of LV during myocardial contraction. A comparison between the circumferential strains during systole in both sets of subjects (Figure 4.20) supports the previous studies results, in which the circumferential stains values are negative during systole, and also the results of the significant ($p<0.05$) lower absolute values on DCM patients, when comparing to healthy subjects.

Moreover, by analyzing the same figure, it is possible to conclude that in healthy subjects, the apical section of LV has the major strain, while in DCM patients, it is the mid section. This was not in agreement with a previous study of depressed contractility in patients with DCM [76], which stated that the major strain in DCM patients was seen in basal area. These strain results may vary due to the difference in the techniques used and to the algorithms to calculate the strains. In that study, the strain was quantified using a standard steady-state in free-precession (SSFP) sequence while this thesis methods only used the SPAMM technique.

Additionally, the effect of gender (male/ female) on the strains was also considered on the DCM patients and the results shown that in women the LV strain is lower than in men. Despite these results, the other studies did not report any conclusions related to this effect. In this case, there was no statistical test due to the low number of female gender subjects, when comparing to subjects with male gender.

After these results, we can conclude that the study of the LV strain is an important parameter in the evaluation of the cardiac contractility. A non-invasive assessment of LV by MRI and the superimposed grid created by SPAMM improved the tracking of LV wall strains. Another conclusion was that the major section responsible for the myocardial deformation was the middle section of the LV. Moreover, it was observed that DCM decreases the deformation capabilities of the heart, as it is responsible for the wall thinning and dilation of heart chambers, causing a decrease in wall radial and circumferential strains.

6. References

[1] http://www.who.int/cardiovascular_diseases/en/ [Accessed: 20/04/2017]

[2] https://www.escardio.org/The-ESC/What-we-do/Initiatives/EuroHeart/2012-European-Cardiovascular-Disease-Statistics [Accessed: 20/04/2017]

[3] Benza, R., Biederman, R., Murali, S., & Gupta, H. (2008). Role of cardiac magnetic resonance imaging in the management of patients with pulmonary arterial hypertension. Journal of the American College of Cardiology, 52(21), 1683-1692.

[4] Phatak, N. S., Maas, S. A., Veress, A. I., Pack, N. A., Di Bella, E. V., & Weiss, J. A. (2009). Strain measurement in the left ventricle during systole with deformable image registration. Medical image analysis, 13(2), 354-361.

[5] https://web.stanford.edu/class/history13/earlysciencelab/body/heartpages/heart.html [Accessed: 20/04/2017]

[6] Saladin, K. S. (2008). The Circulatory System II: Heart. Human Anatomy (4th ed., pp. 572-594) New York, NY: McGraw-Hill

[7] http://www.innerbody.com/image/cardov.html [Accessed: 20/04/2017]

[8] http://biology-forums.com/index.php?action=gallery;sa=view;id=9173 [Accessed: 20/04/2017]

[9] https://www.boundless.com/physiology/textbooks/boundless-anatomy-and-physiology-textbook/cardiovascular-system-the-heart-18/the-heart-172/layers-of-the-heart-walls-864-636/ [Accessed: 26/04/2017]

[10] http://cursoenarm.net/UPTODATE/contents/mobipreview.htm?36/0/36874 [Accessed: 26/04/2017]

[11] https://classconnection.s3.amazonaws.com/875/flashcards/1191875/jpg/picture71333415920480.jpg [Accessed: 20/04/2017]

[12] http://www.medicinenet.com/script/main/art.asp?articlekey=3212

[13] http://philschatz.com/anatomy-book/contents/m46661.html [Accessed: 20/04/2017]

[14] http://classes.midlandstech.edu/carterp/Courses/bio211/chap18/chap18.html [Accessed: 20/04/2017]

[15] http://www.aihw.gov.au/cardiovascular-disease/what-is-cvd/ [Accessed: 20/04/2017]

[16] http://www.world-heart-federation.org/cardiovascular-health/heart-disease/different-heart-diseases/ [Accessed: 20/04/2017]

[17] National Collaborating Centre for Chronic Conditions (Great Britain), & Royal College of Physicians of London. (2003). Chronic Heart Failure: National Clinical guideline for diagnosis and management in primary and secondary care. Royal College of Physicians

[18] http://eurheartj.oxfordjournals.org/content/29/2/270 [Accessed: 20/04/2017]

[19] Sheppard, M. (2011). Practical cardiovascular pathology (pp.152-154) London, CRC Press. Retrieved from http://books.google.com

[20] Beltrami, C. A., Finato, N., Rocco, M., Feruglio, G. A., Puricelli, C., Cigola, E., ... & Anversa, P. (1995). The cellular basis of dilated cardiomyopathy in humans. Journal of molecular and cellular cardiology, 27(1), 291-305.

[21] http://www.wjgnet.com/1949-8462/full/v6/i7/585.htm [Accessed: 20/04/2017]

[22] https://www.youtube.com/watch?v=1E7QZo-JzG [Accessed: 20/04/2017]

[23] Hudsmith, L. E., Petersen, S. E., Tyler, D. J., Francis, J. M., Cheng, A. S., Clarke, K., ... & Neubauer, S. (2006). Determination of cardiac volumes and mass with FLASH and SSFP cine sequences at 1.5 vs. 3 Tesla: a validation study. Journal of Magnetic Resonance Imaging, 24(2), 312-318.

[24] Shah, A. M., & Solomon, S. D. (2012). Myocardial deformation imaging current status and future directions. Circulation, 125(2), e244-e248.

[25] http://circ.ahajournals.org/content/125/3/e267 [Accessed: 20/04/2017]

[26] http://www.mayoclinic.org/tests-procedures/chest-x-rays/basics/why-its-done/prc-20013074 [Accessed: 20/04/2017]

[27] https://radiopaedia.org/cases/normal-frontal-chest-x-ray [Accessed: 20/04/2017]

[28] http://www.heart.org/HEARTORG/Conditions/HeartAttack/DiagnosingaHeartAttack/Cardiac-Computed-Tomography-Multidetector-CT-or-DCT_UCM_446370_Article.jsp#.WB5YWvkgXIU [Accessed: 20/04/2017]

[29] http://www.radiologyassistant.nl/en/p48ce14c4dcd2e/cardiac-anatomy.html [Accessed: 20/04/2017]

[30] Tecelão, S. R. R. (2007). Myocardial strain analysis with high temporal resolution MRI tagging: extended 3D motion tracking in normal and LBBB hearts. (Doctoral dissertation). Retrieved from http://hdl.handle.net/10451/1684

[31] http://jnm.snmjournals.org/content/48/7/1069/F4.expansion.html [Accessed: 20/04/2017]

[32] Tavakoli, V., Bhatia, N., Longaker, R. A., Stoddard, M. F., & Amini, A. A. (2014). Tissue doppler imaging optical flow (TDIOF): A combined b-mode and tissue doppler approach for cardiac motion estimation in echocardiographic images. IEEE Transactions on Biomedical Engineering, 61(8), 2264–2277.

[33] http://radiologykey.com/rheumatic-mitral-valve-disease/ [Accessed: 20/04/2017]

[34] Jerrolds, J., & Keene, S. (2009). MRI safety at 3T versus 1.5 T. Internet J World Health Soc Politics, 6, 1

[35] http://mriquestions.com/gyromagnetic-ratio-gamma.html [Accessed: 20/04/2017]

[36] http://www.brighthubengineering.com/commercial-electrical-applications/122014-physics-of-a-mri/ [Accessed: 20/04/2017]

[37] Muthurangu, V., & Dymarkowski, S. (2011). Cardiac MRI physics. In Clinical Cardiac MRI (pp. 1-30). Berlin, Springer Heidelberg

[38] Berger, A. (2002). How does it work?: Magnetic resonance imaging. BMJ: British Medical Journal, 324(7328), 35

[39] Preim, B., & Botha, C. P. (2013). Visual Computing for Medicine: Theory, Algorithms, and Applications. Massachusets, MA: Newnes

[40] https://www.med-ed.virginia.edu/courses/rad/cardiacmr/Techniques/Physics.html [Accessed: 20/04/2017]

[41] Kim, Y. J., & Mamisch, T. C. (Eds.). (2014). Hip magnetic resonance imaging. Springer New York

[42] https://www.researchgate.net/figure/236931919_fig1_Spin-echo-and-gradient-echo-a-Conventional-spin-echo-pulse-sequence-b-Conventional [Accessed: 20/04/2017]

[43] http://mriquestions.com/does-se-correct-for-t2.html [Accessed: 20/04/2017]

[44] http://www.revisemri.com/questions/pulse_sequences/black_blood_bright_blood.php [Accessed: 20/04/2017]

[45] https://www.med-ed.virginia.edu/courses/rad/cardiacmr/Techniques/SSFP.html [Accessed: 20/04/2017]

[46] https://www.med-ed.virginia.edu/courses/rad/cardiacmr/Techniques/Equipment.html [Accessed: 20/04/2017]

[47] https://mrimaster.com/PLAN%20CARDIC.html [Accessed: 20/04/2017]

[48] Taylor, A. M., & Bogaert, J. (2011). Cardiovascular MR imaging planes and segmentation. Clinical Cardiac MRI (pp. 93-107). Berlin, Springer Heidelberg.

[49] Amini, A. A., & Prince, J. L. (Eds.). (2013). Measurement of cardiac deformations from MRI: physical and mathematical models (Vol. 23). Springer Science & Business Media, 2-10.

[50] Kaplan, J. A., Reich, D. L., & Konstadt, S. N. (2011). Kaplan's Cardiac Anesthesia: Expert Consult Premium. Elsevier Health Sciences, 348-350.

[51] Delgado, V., Ypenburg, C., van Bommel, R. J., Tops, L. F., Mollema, S. A., Marsan, N. A., ... & Bax, J. J. (2008). Assessment of left ventricular dyssynchrony by speckle tracking strain imaging: comparison between longitudinal, circumferential, and radial strain in cardiac resynchronization therapy. Journal of the American College of Cardiology, 51(20), 1944-1952

[52] Geyer, H., Caracciolo, G., Abe, H., Wilansky, S., Carerj, S., Gentile, F., ... & Sengupta, P. P. (2010). Assessment of myocardial mechanics using speckle tracking echocardiography: fundamentals and clinical applications. Journal of the American Society of Echocardiography, 23(4), 351-369.

[53] Cheung, Y. F. (2012). The role of 3D wall motion tracking in heart failure. Nature Reviews Cardiology, 9(11), 644-657.

[54] Yu, W., Li, S. N., Chan, G. C., Ha, S. Y., Wong, S. J., & Cheung, Y. F. (2013). Transmural strain and rotation gradient in survivors of childhood cancers. European Heart Journal-Cardiovascular Imaging, 14(2), 175-182.

[55] Brower, R. W., Harald, J., & Meester, G. T. (1978). Direct method for determining regional myocardial shortening after bypass surgery from radiopaque markers in man. The American journal of cardiology, 41(7), 1222-1229.

[56] Myers, J. H., Stirling, M. C., Choy, M., Buda, A. J., & Gallagher, K. P. (1986). Direct measurement of inner and outer wall thickening dynamics with epicardial echocardiography. Circulation, 74(1), 164-172.

[57] Zerhouni, E. A., Parish, D. M., Rogers, W. J., Yang, A., & Shapiro, E. P. (1988). Human heart: tagging with MR imaging-a method for noninvasive assessment of myocardial motion. Radiology, 169(1), 59-63.

[58] Lima, J. A., Jeremy, R., Guier, W., Bouton, S., Zerhouni, E. A., McVeigh, E., ... & Weiss, J. L. (1993). Accurate systolic wall thickening by nuclear magnetic resonance imaging with tissue

tagging: correlation with sonomicrometers in normal and ischemic myocardium. Journal of the American College of Cardiology, 21(7), 1741-1751.

[59] Meyer, S. A., & Wolf, P. D. (1997). Application of sonomicrometry and multidimensional scaling to cardiac catheter tracking. IEEE transactions on biomedical engineering, 44(11), 1061-1067

[60] Axel, L., & Dougherty, L. (1989). MR imaging of motion with spatial modulation of magnetization. Radiology, 171(3), 841-845

[61] Ibrahim, E. S. H. (2011). Myocardial tagging by cardiovascular magnetic resonance: evolution of techniques–pulse sequences, analysis algorithms, and applications. Journal of Cardiovascular Magnetic Resonance, 13(1), 1.

[62] https://www.med-ed.virginia.edu/courses/rad/cardiacmr/Techniques/Cine.html [Accessed: 26/04/2017]

[63] Alenezy, M. D. (2009). Modeling Left Ventricle Wall Motion Using Tagged Magnetic Resonance Imaging (Doctoral dissertation). Retrieved from https://www.researchgate.net

[64] McVeigh, E. R., & Bolster, B. D. (1998). Improved sampling of myocardial motion with variable separation tagging. Magnetic resonance in medicine, 39(4), 657-661

[65] Valeti, V. U., Chun, W., Potter, D. D., Araoz, P. A., McGee, K. P., Glockner, J. F., & Christian, T. F. (2006). Myocardial tagging and strain analysis at 3 Tesla: comparison with 1.5 Tesla imaging. Journal of Magnetic Resonance Imaging, 23(4), 477-480.

[66] Liu, W., Chen, J., Ji, S., Allen, J. S., Bayly, P. V., Wickline, S. A., & Yu, X. (2004). HARP MRI tagging for direct quantification of Lagrangian strain in rat hearts after myocardial infarction. Journal of biomechanical engineering, 126(4), 523

[67] Osman, N. F., Kerwin, W. S., McVeigh, E. R., & Prince, J. L. (1999). Cardiac motion tracking using CINE harmonic phase (HARP) magnetic resonance imaging. Magnetic resonance in medicine: official journal of the Society of Magnetic Resonance in Medicine/Society of Magnetic Resonance in Medicine, 42(6), 1048.

[68] Osman, N. F., & Prince, J. L. (2000). Visualizing myocardial function using HARP MRI. Physics in medicine and biology, 45(6), 1665.

[69] http://www.iacl.ece.jhu.edu/static/harp/ [Accessed: 26/04/2017]

[70] Haber, I., & Westin, C. F. (2002). Model-based 3D tracking of cardiac motion in HARP images. ISMRM; Honolulu, HI.

[71] Pan, L., Lima, J. A., & Osman, N. F. (2003, July). Fast tracking of cardiac motion using 3D-HARP. In Biennial International Conference on Information Processing in Medical Imaging

(pp. 611-622). Springer Berlin Heidelberg.

[72] Garot, J., Bluemke, D. A., Osman, N. F., Rochitte, C. E., McVeigh, E. R., Zerhouni, E. A., ... & Lima, J. A. (2000). Fast determination of regional myocardial strain fields from tagged cardiac images using harmonic phase MRI. Circulation, 101(9), 981-988.

[73] Bin, L., & Yeganeh, M. S. (2012). Comparison for image edge detection algorithms. IOSR Journal of Computer Engineering, 2(6), 1-4.

[74] http://www.pmod.com/files/download/v34/doc/pcardp/3615.htm[Accessed: 26/04/2017]

[75] http://mriquestions.com/polar-plots.html [Accessed: 26/04/2017]

[76] Taylor, R. J., Moody, W. E., Umar, F., Edwards, N. C., Taylor, T. J., Stegemann, B., ... & Leyva, F. (2015). Myocardial strain measurement with feature-tracking cardiovascular magnetic resonance: normal values. European Heart Journal–Cardiovascular Imaging, 16(8), 871-881.

[77] Duan, F., Xie, M., Wang, X., Li, Y., He, L., Jiang, L., & Fu, Q. (2012). Preliminary clinical study of left ventricular myocardial strain in patients with non-ischemic dilated cardiomyopathy by three-dimensional speckle tracking imaging. Cardiovascular Ultrasound, 10(1), 8.

[78] MacIver, D. H., Adeniran, I., & Zhang, H. (2015). Left ventricular ejection fraction is determined by both global myocardial strain and wall thickness. IJC Heart & Vasculature, 7, 113-118.

[79] Yingchoncharoen, T., Agarwal, S., Popović, Z. B., & Marwick, T. H. (2013). Normal ranges of left ventricular strain: a meta-analysis. Journal of the American Society of Echocardiography, 26(2), 185-191.